

ISSN:2538-516X

Journal of  
**Civil  
Engineering  
Researchers**

Volume: 4; Number: 2; June 2022

Chief Editorial:  
Morteza Jamshidi

Managing Editor:  
Kamyar Bagherineghad



**J-Researchers**



**Volume 4, Number 2, June 2022**

## **Contents**

1. **Investigation of the effect of offshore fixed wind turbine blades on fatigue damage of bases in the Hengam region in Iran** 1-11  
Yeganeh Jahandar, Saleh Aminyavari, Akbar Shahidzadeh Arabani
2. **Experimental evaluation of compressive, tensile strength and impact test in blast furnace slag based geopolymer concrete, under high temperature** 12-21  
Mohammadhossein Mansourghanaei, Morteza Biklaryan
3. **Study on the Performance of High-Strength Steel Shear Wall with Opening and Pre-crack** 22-33  
Mohammad komeil Sadeghi golafshani
4. **Pervious concrete as environmentally friendly materials-an overview** 34-40  
Shahriar gholamin
5. **The effect of steel and hybrid fibers on the impact resistance of concrete enclosed with FRP sheets** 41-45  
Zahed Parvinnejad
6. **Study of the collapse of Sardabroud-Chalous truss bridge** 46-51  
Morteza Jamshidi, Teymour Sam



## Investigation of the effect of offshore fixed wind turbine blades on fatigue damage of bases in the Hengam region in Iran

Yeganeh Jahandar <sup>a</sup>, Saleh Aminyavari <sup>a,\*</sup>, Akbar Shahidzadeh Arabani <sup>a</sup>

*Department of Civil Engineering, Chalous Branch, Islamic Azad University, Chalous, Iran*

**Article History:** Received date 2022.04.08; revised date : 2022.05.24; accepted 2022.09.25

---

### Abstract

Today, wind energy is considered as one of the most used types of renewable energy for electricity production. Over the past two decades, wind energy has been a major source of electricity, and electricity supply has been drastically increasing. Among the technologies available to generate electricity from wind, wind turbines play a major role, with offshore wind turbines playing a significant part. Offshore structures such as wind turbines, unlike other types of structures, are in a dynamic environment, the main forces generating this dynamic wave and wind environment, which impose significant structural vibrations, fatigue loads and significant loads on the blades, the turbine, structural platform, and other components import it. Welded joints and points in offshore structures are vulnerable to fatigue failure due to stress concentrations and intermittent environmental loading. Offshore structures have been exposed to shock forces and cyclic loads throughout their lifetimes, which cause the cyclic loads to cause fatigue in the joints. The dynamic forces of the waves gradually cause small cracks in the structural joints over time, and the expansion of these cracks at the weld foot and joints of the structural members reduces the overall stiffness of the joint and in some cases even removes the member from the location of connection. Much research has been done on the use of offshore wind energy, but despite the special attention of the worldwide scientific community on offshore wind energy extraction, there are still few studies domestically. Considering the water levels in the south of Iran and the platforms in the area will add to the importance of this study. The turbine structure will be examined to perform the research by using and inspiring DNV and API by-laws when the method is nonlinear. The case study will also cover the Strait of Hormuz and the time zone. This research is carried out using coding in Matlab as well as analysis in Bentley SACS finite element software which is dedicated to the design of offshore steel structures. The results indicate that the presence of the turbine blade geometry has a significant effect on the fatigue life of the retaining structure and the entire structure. (DOI:<https://doi.org/10.52547/JCER.4.2.1>)

**Keywords:** Blades, Offshore, Wind Turbines, Fatigue Damage, Hengam

---

\* Corresponding author. Tel.: +989112912393; e-mail: saleh1161a@gmail.

## 1. Introduction

Over the past two decades, wind energy has received a great deal of attention as a source of electricity, and the supply of electricity using this source is increasing rapidly. Among the existing technologies for generating electricity from wind, wind turbines play the main role, among which offshore wind turbines play a significant part of this role, the attention to this part is increasing daily. Offshore structures such as wind turbines, unlike other types of structures, are in a dynamic environment, the main forces creating this dynamic environment are waves and winds, these forces, structural vibrations, fatigue loads and significant heavy loads to the blades. They import turbines, structural platforms, and other components. According to the mentioned conditions, today, the installation of offshore platforms in very deep waters and very unfavorable environmental conditions is also economically justified. Therefore, at present, extensive and increasing efforts are underway to provide solutions for the analysis and design of offshore structures against a variety of destructive phenomena, including the phenomenon of fatigue. Welded joints and joints in offshore structures are vulnerable to fatigue rupture due to stress concentrations and periodic environmental loading. One of the most important factors in immediate failure as well as reducing the strength of offshore platforms in the long run is the phenomenon of fatigue in the joints and structural members.

Wang et al. (2016) presented a stochastic dynamic response analysis for a 5MW vertical-axis floating wind turbine as a completely nonlinear coupling in the time domain. The FVAWT studied in this research, which is a combination of a Daris rotor and a semi-submersible float, is placed under different wind and wave conditions, and its overall motion, structural response, and elongation of inhibitory lines are simulated in the time domain as well as the domain. Frequency is obtained. In this research, the response of FVAWT in uniform and turbulent wind conditions is compared and the superiority of this type of turbine over the model with its fixed base in

reducing the effect of  $2p$  on the dynamic response is shown [1].

Skaare et al. (2015) performed a comparative analysis between measurements made on the Hywind floating wind turbine main scale sample and its numerical simulations. In this study, they described the main characteristics of the Hywind structure, its control system and the important measurements made. In this research, a method for estimating the impact wave level to the Hywind structure is proposed and dynamic simulations comparable with the estimated time levels of the estimated wave level along with the measured statistical parameters of the wind field have been performed. Finally, the measured values of movement of roll, screw and yaw modes, tower bending torques, traction line tension, power generation, rotor speed and blade angle in both wind speeds lower and higher than the operating speed with simulations Numerical performed by SIMO / RIFLEX / HAWC2 numerical tool has been compared and has shown a very good fit [2]

Zhang et al. (2015) simulated the floating section and bracing system of a spar floating wind turbine with chain harness using Orcaflex software. In this research, by calculating the loads on the wind turbine, hydrodynamic analysis has been performed on the braking system and the tension of the braking lines under different loading conditions has been studied. Finally, using the obtained results, an optimal design for the desired inhibition lines was presented [3]

In 2016, Tamamgar et al. Feasibility study and location of offshore wind turbine fields on the shores of the Persian Gulf and the Sea of Oman, along with providing the optimal option of the basic turbine infrastructure and the optimal pattern of arrangement and arrangement of fields. In this study, after zoning, which is necessary to start a coherent research, wind information related to the southern regions of the country for 7 years, including the years 2000, 2005 and 2009 to 2013 were collected, and after classification and the creation of a data center Can be used for future work, annual averaging and determining the feasibility criteria of the regions according to the IEC standard, the study of the wind pattern of the region was performed to validate the information used. Also, at this stage of the research, it was found that there are compatible wind turbines on the mass production scale for the mentioned

region as well as regions with slightly lower speeds. In the next step, while introducing the types of fixed infrastructure used in the offshore wind industry and classifying their strengths and weaknesses, through a scoring system according to studies and considering the approximate depth of the potential area, which is approximately 50 meters, Jacket infrastructure was identified as suitable infrastructure [4]. Also, Baroni et al. (2016) Presented research entitled Dynamic Response Analysis of Offshore Floating Wind Turbines. In the present study, the motion responses for operating conditions have been investigated to evaluate the performance and structural stability of Spar floating wind turbine with chain restraint. To develop powerful design tools for the offshore wind industries, modeling requirements have been determined and the dominant physical processes have been calculated, and subsequently the BA-Simula model has been developed. Finally, the results obtained in the field of time and frequency are presented and using various validation methods, it is shown that the BA-Simula model simulates different loads well and can be a useful tool for estimating the physical behavior of the turbine. Floating wind turbines [5].

As the share of wind in the production of human energy is increasing, so are offshore wind turbine farms. An offshore wind turbine must be able to withstand the sea environment, which consists of wind and wave loads. The wind and wave create significant vibrations in the turbine structure and cause fatigue loads on the blade, the base of the structure and other turbine components. Fatigue loads increase maintenance operations, reduce turbine access, use expensive components, and ultimately break down turbine structures. Structure control technique can be used to reduce turbine vibrations and fatigue loads. So far, little scientific and laboratory research has been done in this field. Matthew et al. Investigated the passive control of offshore wind turbines and used mass dampers to control structural responses. A code called Fast is used to analyze the turbine. This is a program code written in the National Renewable Energy Laboratory. Also, for modeling the tuned mass damper (TMD), the Fast program was developed by Lackner and Rotea (2011) And is known as Fast-SC. In this research, a barge and monopile turbine have

been investigated. The results of this study show that the use of a TMD damper controls the turbine responses to incoming loads and thus reduces the turbine vibrations [6]

Hu and He (2017) Examined the semi-active control of floating base turbines. In this research, an adjustable fluid column damper has been used to control the turbine vibrations. In this research, infinite H algorithm is used to obtain feedback. The results of this study show that the application of liquid column dampers improves the performance of the turbine in the face of completely dynamic sea conditions and the vibrations of the structure are well controlled. [7].

Colwel and Basu (2009) Also investigated the structural control of offshore wind turbines using liquid column dampers. In this study, the turbine has been modeled as a multi-degree of freedom structure. The Kaimal and JONSWAP spectra have been used to model wind and wave load, respectively. The results of this study show that with the use of liquid column dampers, the maximum response of the structure is reduced by about 55%. This reduction in turbine structure vibrations reduces turbine construction costs. Also, increasing the damper amplitude increases the fatigue life of turbine components [8].

In research by Thompson and Sørensen (1999), an increase in fatigue load in the wind farm compared to free flow was found between 5 and 15% depending on the wind farm design. The increase in load because of awakening was the same for a marine and terrestrial site [9].

Hakmabadi et al., (2016) investigated the application of a tuned mass damper with different masses, in an offshore Tension Leg Platform (TLP). Tuned Mass Dampers (TMDs) modeled in a developed code FAST-SC. Results show that using TMD in the nacelle can reduce the moments in the base of the tower and turbine vibration. This reduction can also increase time until failure factor of the OWTs. [10].

## 2. Methodology

The information corresponding to the specifications of the wind turbine support structure

studied in this region is given in Table 1. It is worth mentioning that 5 class levels have been considered to investigate the phenomenon of fatigue in this study, of which 3 class levels are below the water level and 2 class levels are above the base level.

Table 1  
Specifications of wind turbine holding structure studied in this area

Water depth at the place of installation of wind turbine structure	61.5 meters
Height of wind turbine jacket to the bottom of the sea	81 meters
Base of the structure	140 cm diameter, thickness 2.5 cm
Details of class levels	+9, +5.75, -6, -18-, -37.5
Angle of sea waves entering the structure of wind turbine holder	45° (8 directions)
specific gravity of water	$\rho=1025 \text{ kg/m}^3$

In this research, the material of the supporting structure and wind turbine will be strong steel. The specifications of the materials in the steel section of the structure will be as shown in Table 2.

Table 2  
Characteristics of materials used in the case platform model

Special Weight (kN /cm <sup>2</sup> )	yield stress (kN /cm <sup>2</sup> )	Shear modulus (kN /cm <sup>2</sup> )	modulus of elasticity (kN /cm <sup>2</sup> )
7850	35.50	7921	20590

To apply the loading section to the wind turbine structure under study, information obtained from design companies as well as experts and specialists should be provided. Among these, data such as wind information from different geographical directions,

water depth and storm wave data, 1-year and 100-year wave information, and flow information are in the focus of considerable importance.

In the following, in Table 3, the information corresponding to the wind speed that occurred in the Hengam area in the 1-year operating conditions and the so-called 100-year emergency conditions are listed.

Table 3  
Water depth, storm surge and wind speed in Hengam Region

Parameter	Depth (m)							
	SE	E	NE	N	NW	W	SW	S
LAT above seabed	61.5							
MHHW above LAT	1.6							
Storm surge (100 yrs)	0.3	0.2	0.1	0.1	0.3	0.2	0.1	0.2
Storm surge (1 year)	0.2	0.1	0.1	0.1	0.2	0.1	0.1	0.1
Total SWL (100 yrs)	63.4	63.3	63.2	63.2	63.4	63.3	63.2	63.3
Total SWL (1 year)	63.3	63.2	63.2	63.2	63.3	63.2	63.2	63.2
	Wind speed (m/s)							
	SE	E	NE	N	NW	W	SW	S
Wind speed (1 year)	21.7	22.2	21.5	27.6	22.7	22	20.4	20.6
Wind speed (100 yrs)	35.2	36	34.9	35.6	36.7	35.6	33	33.4

Water depth and storm wave data of the region When in the path of digitization and completion of depth data in the study area, the base level around the LAT level is 61.5 meters. This level is the lowest level of the astronomical tide from the seabed to the water level. Also, the value corresponding to MHHW (Mean Higher High Water) above the LAT level is 1.6 meters. Storm wave values as well as total water levels for 1-year operating conditions and so-called 100-year emergency conditions are also listed.

The wave information of the study area includes the characteristic wave height (in meters) and the wave period (in seconds) in the case of one-year and 100-year return periods in different directions of

application according to Table 4. As can be seen from the table, the minimum value of the characteristic wave height for a one-year return period is from the southwest direction by 5 meters and the maximum value is 6.7 meters from the northwest direction. The mentioned values correspond to the 100-year return period are 8.8 meters from the southwest and northeast and 12.2 meters from the northwest, respectively.

Table 4  
1-year and 100-year wave information

Parameter	Wave (1 year)							
	SE	E	NE	N	NW	W	SW	S
Height (m)	6.3	6	5.1	5.5	6.7	6	5	5.6
Period (s)	8.3	8.1	7.5	7.8	8.6	8.1	7.4	7.9
	Wave (100 yrs)							
	SE	E	NE	N	NW	W	SW	S
Height (m)	11.6	10.8	8.8	9.7	12.2	10.8	8.8	10.2
Period (s)	10.8	10.4	9.6	10	11	10.4	9.5	10.2

Flow data Operational and extraordinary conditions for the Hengam area in both bed conditions are considered as rough and flatbed conditions in explaining the flow force. Also, 4 selected levels to provide a more tangible relationship with this phenomenon in the study environment are presented. These 4 levels include the current at the surface, the current at medium height, the current at a depth of 1 meter from the seabed and the current at a depth of 0.5 meters above the seabed. It is necessary to mention that to create a reliability coefficient in the design, the amount of flow velocity at the middle height is equal to the amount of flow at the surface. These values are given in Table 5 in full. The flow velocity in this research is considered in meters per second.

Table 5  
Flow information

Flow condition	Flow velocity in rough bed	Flow velocity in flat bed
Surface flow	0.9	1.28
Flow in middle height	0.9	1.28
1 meter above the seabed	0.68	0.78
0.5 meter above the seabed	0.62	0.71

## 2.1. The Coefficient of Morrison equations

Wave force calculations are divided into two categories. In small platforms or platforms that are installed in relatively shallow water, the design related to the wave forces is done by loading static forces on the structure. In taller structures where the natural period of vibration of the structure is closer to the period of sea waves, a complex dynamic analysis must be performed. In this article, only static design is studied. Wave design forces should be considered based on the worst conditions caused by hurricanes with a return period of 111 years. In calculating the water depth in the storm mode, high storm waves with normal tides should be considered. The design wave for static analysis of waves is determined by the client whose structure is designed to his order. The horizontal force exerted by the waves on a cylindrical member consists of two parts, one is the drag force from the kinematic energy of water and the other is the inertial force from the acceleration of water particles. To obtain the total force on a member, the water pressure is multiplied by the volume or area of the member image perpendicular to the direction of the wave current. This force is calculated along the member unit using the relation provided by Morison, O'Brien, Johnson, and Schaaf, 1950. This relationship of force on a pipe result in two components, inertia, and drag. This relationship is as follows:

$$F = F_I + F_D \quad (1)$$

$$F = C_m \frac{w\pi D^2}{g} \frac{du}{dt} + C_d \frac{1}{2} \frac{w}{g} Du|u|$$

The values of  $cm$  and  $cd$  are obtained through experiments and modeling, depending on the shape and size of the tube, the amount of mass added to it in water, and the type of wave theory used to calculate the velocity and acceleration of water particles has it. In this study, the drag and inertia coefficients  $cm$  and  $cd$  in Morison relation are considered according to Table 6. These coefficients will be dimensionless.

Table 6  
Drag and inertia coefficients

Members	$C_{dN}$	$C_{mN}$
Flat tube members	1.6	1.6
Smooth tube members	0.65	1.6
Coarse tube members	1.05	1.20

### 2.2. Effect of growth on the surface of the structure

Due to the difference in thickness created by the growth of seaweed on the cross section of the offshore wind turbine body structure and its effect on the coefficients and values of the Morrison equation, this parameter will be one of the components affecting the research results. This item is considered in two parts. Thus, from the class level of +2 to the class level of -6, a section and from the class level of -6 to the mudline are considered as the second section. The amount of thickness added to different parts of the wind turbine base is according to Table 7.

Table 7  
Amount of thickness added to different parts of the wind turbine

Thickness	Elevation	Dry density
Radius 75 mm	+2 to -6	1400 kg/m <sup>3</sup>
Radius 75 mm decreasing to 50 mm	-6 to mudline	

### 2.3. Modeling of wind turbine implementation

Analysis of wind turbine structure using three-dimensional model includes support structure and deck, outer cylinder of wind turbine and wind turbine blades. Accessories such as shock absorbers and floating landings are also installed to calculate the peripheral loads. The structure under study is explained in the part of the support body and the deck of the turbine. Information about situations such as the introduction of middle floor levels, level change angle of structural foundations, bed level, pile, and

deck connection section, piling specifications of the structure are provided in this section.

In the following, the specifications of the wind turbine structure foundations are mentioned in terms of the number and rows of calls to the software, the slope of the foundations and the state of pile and base interference. It is worth mentioning that the supporting structure will be considered as 3 bases. In the next stage of design, the dimensions of structural sections, structural joints and details of loading sections will be considered. In the following and in Figure 1, the wind load loading conditions are given in the selected direction of zero degrees with a velocity of 27.6 meters per second. The three-dimensional schematic shown in the figure shows the details of the offshore wind turbine support structure in sections such as the work point, Fender.



Figure. 1. Applying wind force to the structure

According to Figure 2 simultaneously, the profile corresponding to the application of wave force and current on the structure is presented.



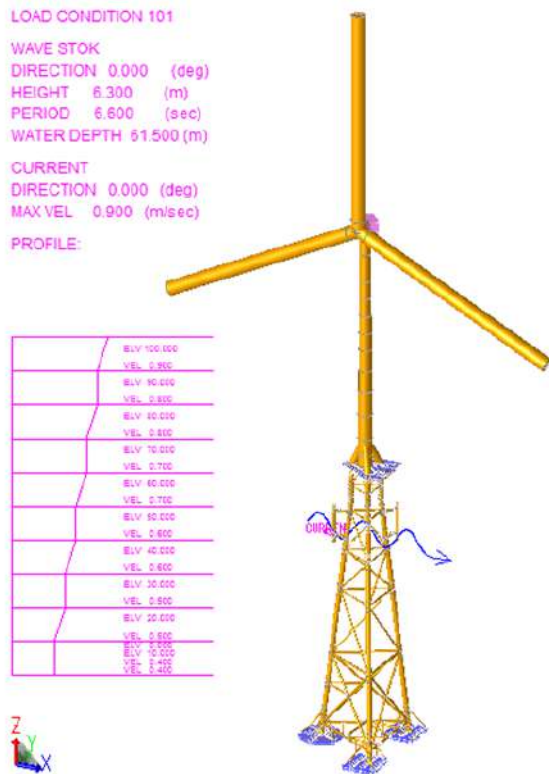


Figure. 2. Simultaneous application of wave force and current on the structure

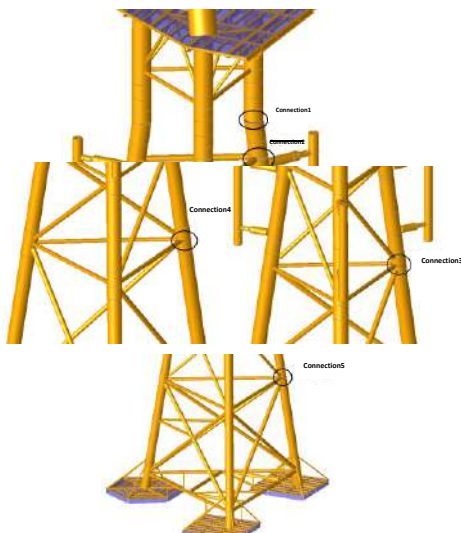


Figure. 3. Connection1 at level -6 meters above water level and connection2 at level +5.8 meters, Connection3 at level +9 meters above water level, connection4 at level -18 meters and connection5 at level -37 meters relative to water level

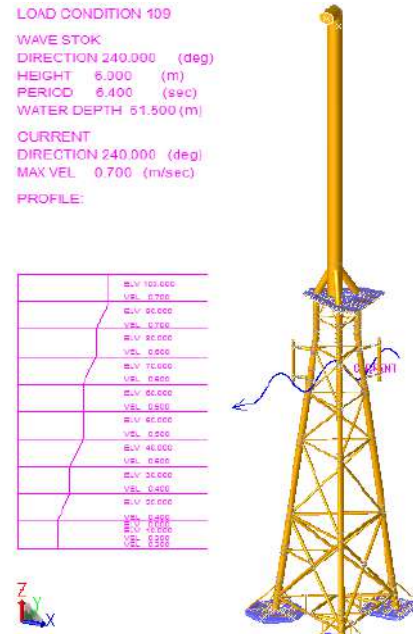


Figure. 4. Simultaneous application of wave force and current on a bladeless structure

#### 2.4. Fatigue analysis method used in the research

As mentioned, to calculate the fatigue damage inside the structure, several methods can be calculated. In this research, we use the Determinant method. Determinant analysis is in fact static in nature and the dynamic properties of the structure are considered in a dynamic incremental coefficient.

In the first stage, by solving the wave equation, the velocity and acceleration of the particles are stored as a function of the depth and angle of the wave phase in a matrix so that these data can be used in the next step.

In the second stage, the geometry and dimensions of the structure are received as input and using the Morrison equation, the wave force is applied as a wide load on the structure and the wave load is converted to knot forces. At this stage, the wave

phase angle is changed from zero to 360 degrees and in each phase angle, according to the position of the relevant element relative to a base point (zero coordinates of the structure), the wave force is converted to nodal forces in structural analysis. To be used.

At the end of the second stage, the wave force in all members is converted to nodal loads and used in the matrix of stored nodal forces in structural analysis.

In the third stage, first, by performing an analysis of special values in the structure, the periodicity of the structure is used and according to the periodicity of the wave and the structure, the Dynamic Amplification Coefficient (DAF) will be calculated.

$$DAF = \frac{1}{\sqrt{[1 - (\frac{TS}{TW})^2]^2 + [2\xi(\frac{TS}{TW})]^2}} \quad (2)$$

Table 8

Natural Periods of Jacket Platform

MODE	FREQ.(CPS)	GEN. MASS	EIGENVALUE	PERIOD(SECS)
1	0.408745	2.7393324E+03	1.5161241E-01	2.4465115
2	0.619758	2.8726531E+03	6.5947035E-02	1.6135318
3	0.622837	1.64413069E+03	6.5296797E-02	1.6055573
4	2.129900	1.7763440E+03	5.5836977E-03	0.4695057
5	2.195281	1.4941853E+03	5.2560553E-03	0.4555225
6	2.866091	2.4158849E+03	3.0836153E-03	0.3489072
7	2.944449	3.9777338E+02	2.9216777E-03	0.3396222
8	3.007557	4.7962469E+01	2.8003514E-03	0.3324958
9	3.327140	2.8971882E+01	2.2882213E-03	0.3005584
10	3.431388	2.1694043E+03	2.1512974E-03	0.2914272

Table 9

The force and moment on the structure of the first state jacket with vertical bases

BASE SHEAR AND OVERTURNING MOMENT COEFFICIENTS				
MODE	SHEAR(X) KN	SHEAR(Y) KN	MOMENT(X) KN-M	MOMENT(Y) KN-M
1	-1351.462	-1.772	-34.303	15597.192
2	1.779	-1864.761	-24285.719	-7.030
3	9.535	-35.679	4556.879	-1478.847
4	4.618	-4260.251	-448642.306	-207.627
5	-4979.908	-1.925	-195.807	476287.867
6	-105.461	-198.077	-11200.575	10940.278
7	-2003.320	-64.148	-4014.283	-11837.978
8	-169.663	1390.891	83878.865	19560.346
9	-11.175	-6780.121	-336782.681	3538.965
10	-5850.145	47.073	5050.972	162775.367

We considered the structural modes to be ten, the first three modes being the most important mode, and the period of the structure with angle-free bases being 2.446 seconds, which is in accordance with the standard API regulations and less than three seconds. Which is mentioned in the regulations for the Persian Gulf region.

In the fourth stage, using the matrix of node forces obtained from the second stage and the dynamic amplification coefficient obtained from the third stage, structural analysis is performed in the structure using SACS software [11] and the forces in the members leading to the connection will be stored at all angles of the wave phase.

In the fifth stage, according to the connection geometry and members, the stress coefficients in each connection are obtained and by using the forces obtained from the fourth stage, the stress in the inflamed area in all the restraints of the connection on both sides of the restraint and the main member will be obtained. In each connection, the maximum and minimum stress will be selected from all angles of the wave phase by maintaining its algebraic sign, and by using these two values, changes in the stress interval in each connection will be obtained.

In the sixth step, according to the values of stress efficiency obtained in each joint using the stress-life curve, the maximum number of tolerable cycles within the joint is determined and according to the number of load cycles in the structure and according to Palmgren-Miner Rule [12], fatigue damage accumulation in the structure will be calculated. The wave scatter diagram in the fatigue life evaluation is shown in the table below.

Table 10

Magnification coefficient correction for 1-year and 100-years

Wave direction	1-year	DAF 1-year	100-years	DAF 100-years
West	8.1	1.0426	10.4	1.023
Southwest	7.4	1.0514	9.5	1.03
South	7.9	1.0448	10.2	1.026
Southeast	8.3	1.040	10.8	1.023
East	8.1	1.0425	10.4	1.025
Northeast	7.5	1.05	9.6	1.029
North	7.8	1.046	10	1.027
Northwest	8.6	1.037	11	1.022

The desired life of the design, which is recommended in the API regulations for the life of the jacket platform bases based on 50 years, must be defined. In the theory of irregular waves, there are various spectrums that used the Pearson Moskvich spectrum.

To establish a more tangible relationship with the current phenomenon under study, in Figure 5, the current force profile on the platform is drawn. The values of flow velocity are not zero at the bed level and have a value of 0.69 m/s, and as we get closer to the surface, this value increases and changes in a parabolic manner.

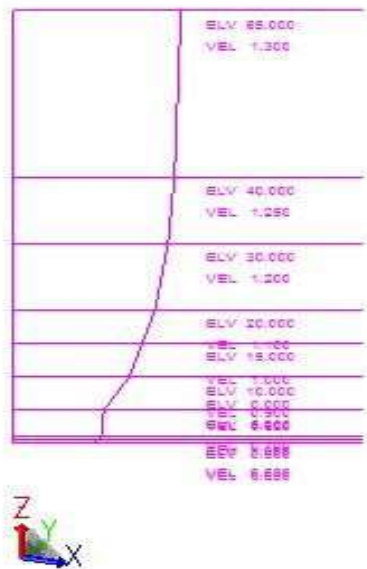


Figure. 5. Profile of the current force acting on the platform

As previously mentioned, the platform studied in this research is a 4-base jacket platform and the order of numbering the platform bases is as follows.

It is worth mentioning that base-1 and 2 - 3 and 4 are of the same type and the characteristics of the material and the base angle (1 and 2), (3 and 4) each are equal. In this issue, due to the large volume of results and the duration of finite element software in this research, we examine the first and third bases. Base number two has the same results as base number one and base number four has the same results as base three. In the following, we considered four connections in the level of each floor. We

considered the location of these connections as the connection of the class level to the base of the platform (joint) as shown in Figure 6. The reason for choosing this place is that punching is done in this area, and it is one of the most critical connections.

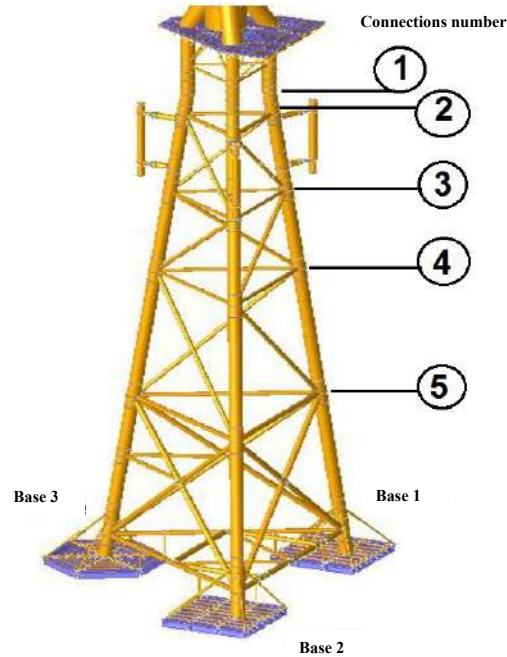


Figure. 6. Numbering the bases of the wind turbine holding structure

### 3. Result

After performing several analyzes on both output modes, the fatigue damage is attached to the following.

Table 11

Calculation of fatigue damage in four base connections 1 and 2 in platform mode with pile-soil interaction

*** HERRER FATICUE REPORT ***											
(JOINT NUMBER)											
JOINT	MEMBER	GROUP	TYPE	ORIG. CO. (CM)	WT. (CM)	JNT. HEM. (N)	LEN. (M)	GRP. * STRESS CONC. FACTORS *	FATIGUE RESULTS		
ID	ID	ID	ID					NO-ER	NO-SI	IN-PL	NO-PL
1001	1001-0000	CL	TUB	170.00	5.00	F	25.28	2.00	2.00	2.00	2.00
1002	1002-0000	CL	TUB	170.00	5.00	F	20.55	2.00	2.00	2.00	2.00
1003	1003-0000	CL	TUB	170.00	5.00	F	25.28	2.00	2.00	2.00	2.00
1004	1004-0000	CL	TUB	170.00	5.00	F	20.55	2.00	2.00	2.00	2.00

Table 12

Calculation of fatigue damage in four base connection1 in platform mode without pile-soil interaction (seabed rigidity)

*** MEMBER FATIGUE REPORT *** (JOINT ORDER)														
JOINT	MEMBER GROUP	TYPE	ORIGIN ID	VT (CM)	HT (CM)	HT (CM)	LEN (M)	GAP	STRESS CONC. FACTORS	FATIGUE RESULTS				
			ID						AS-CH AS-SB IN-PL OUT-PL	DAMAGE LOC	SRC	SRG	SRG	SRG
1001	1001-3400	CLH	T00	170.00	5.00	V	20.55	2.00	2.00 2.00 2.00	1.000718	I	73.47504		
1001	1001-3400	CLH	T00	170.00	5.00	V	20.55	2.00	2.00 2.00 2.00	.9450520	TR	77.99029		
1001	1001-3400	CLQ	T00	170.00	5.00	V	20.55	2.00	2.00 2.00 2.00	.4726308	I	158.51604		
1001	1001-3400	CL	T00	170.00	5.00	T	20.41	2.00	2.00 2.00 2.00	.4402021	B	127.3259		

Table 13

Calculation of fatigue damage in four base connection1 in platform mode without pile-soil interaction (seabed rigidity)

*** MEMBER FATIGUE REPORT *** (JOINT ORDER)														
JOINT	MEMBER GROUP	TYPE	ORIGIN ID	VT (CM)	HT (CM)	HT (CM)	LEN (M)	GAP	STRESS CONC. FACTORS	FATIGUE RESULTS				
			ID						AS-CH AS-SB IN-PL OUT-PL	DAMAGE LOC	SRC	SRG	SRG	SRG
2001	2001-3400	CLH	T00	170.00	5.00	V	20.55	2.00	2.00 2.00 2.00	1.207619	B	61.99594		
2001	2001-3400	CLH	T00	170.00	5.00	V	20.55	2.00	2.00 2.00 2.00	.9401229	TR	77.95202		
2001	2001-3400	CLQ	T00	170.00	5.00	V	20.55	2.00	2.00 2.00 2.00	.9999430	R	75.00020		
2001	2001-3400	CL	T00	170.00	5.00	T	20.41	2.00	2.00 2.00 2.00	.8402940	B	89.55945		

Table 14

Calculation of fatigue damage in four connections of base3 in platform mode without pile-soil interaction (seabed rigidity))

*** MEMBER FATIGUE REPORT *** (JOINT ORDER)														
JOINT	MEMBER GROUP	TYPE	ORIGIN ID	VT (CM)	HT (CM)	HT (CM)	LEN (M)	GAP	STRESS CONC. FACTORS	FATIGUE RESULTS				
			ID						AS-CH AS-SB IN-PL OUT-PL	DAMAGE LOC	SRC	SRG	SRG	SRG
3001	3001-3400	CLH	T00	170.00	5.00	V	20.55	2.00	2.00 2.00 2.00	1.209256	TR	62.18050		
3001	3001-3400	CLH	T00	170.00	5.00	V	20.55	2.00	2.00 2.00 2.00	.9403027	TR	78.09379		
3001	3001-3400	CLQ	T00	170.00	5.00	V	20.55	2.00	2.00 2.00 2.00	.5445189	I	137.7330		
3001	3001-3400	CL	T00	170.00	5.00	T	20.41	2.00	2.00 2.00 2.00	.5445189	B	147.5475		

### 3.1. Validation of output results

At the end of the research, to validate the research and in fulfilling the validation item, the amount of fatigue life obtained in the connections of the jacket platform bases will be examined and compared with the valid API regulations [13]. The paragraph used is as shown in Figure 7.

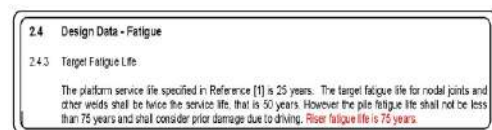


Figure. 7. Paragraph used in the API regulations

Figure 8 shows that the results are acceptable for the fatigue design life of the platform joints (50 years).

## 4. Conclusion

In this research, a structure with the use of non-fossil and natural wind energy extraction is made of four separate structures, which include the deck of the structure in the form of a cylinder and wind turbine as the main part of the research, retaining structure and piles buried in the seabed. Usually, most of such research have omitted the presence of the candle section and have considered the seabed rigidly, but in this dissertation, the existence of a candle has also been considered and the seabed has been considered as elastic.

Considering the interaction of piles, soil and supporting structures with wind turbines and cylinders connected to it for some analyzes including fatigue analysis, earthquake analysis, static structure analysis, dynamic structure analysis, ship impact analysis and even important material analysis will be.

After one of the wind turbine structures in Hengam area located in the Strait of Hormuz and the southern part of Qeshm Island, was considered, the fatigue analysis of the body of this wind turbine structure with the presence of piles and soil was done



by time history method and main outputs Achieved and attached.

The minimum fatigue life designed for the bases of wind turbine structures in the API regulations is based on 50 years, the service life for the first and second base in four class levels is a maximum of 108 years and a minimum of 68 years, and life Service for grades three and four in four class levels is a maximum of 93 years and a minimum of 62 years.

As can be seen, the closer we get to the seabed level, the less wave and current force and the longer the service life at lower levels, and vice versa, the closer we get to the water level, the higher the wave and current force reached, and the service life is reduced. This issue is briefly at the wave and current profiles and the collision with the structure is completely transparent, which is mentioned in most marine structural engineering references.

As can be seen, the minimum design life of wind turbine structure foundations is longer than the life recommended in the regulations.

In explaining the fatigue phenomenon of offshore structures such as wind turbines and fixed platforms, the time history method is more accurate than the definite method, because, in the time history method, the structure is studied hydrodynamically, but in the definite method in static form. As a result, the results of time history analysis outputs are closer to reality.

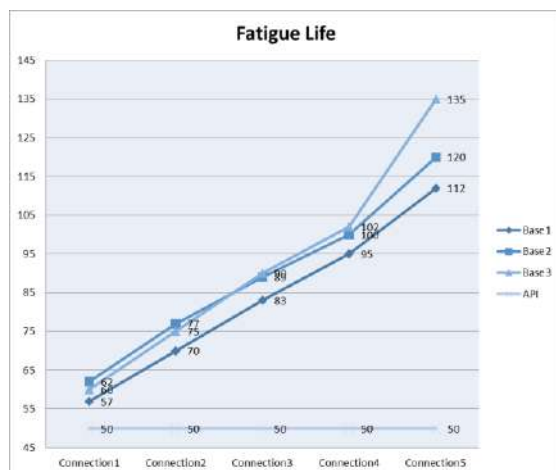


Figure.8 Validation of model results

## References

- [1] Wang, K., Moan, T., & Hansen, M. O. (2016). Stochastic dynamic response analysis of a floating vertical-axis wind turbine with a semi-submersible floater. *Wind Energy*, 19(10), 1853-1870.
- [2] Skaare, B., Nielsen, F. G., Hanson, T. D., Yttervik, R., Havmøller, O., & Rekdal, A. (2015). Analysis of measurements and simulations from the Hywind Demo floating wind turbine. *Wind Energy*, 18(6), 1105-1122.
- [3] Zhang, D. P., Zhu, K. Q., Jing, B., Yang, R. Z., & Tang, Z. C. (2015). Dynamic analysis of the mooring system for a floating offshore wind turbine spar platform. *International Conference on Computer Information System AND industrial Applications*, 3(3.5), 1.
- [4] Tamamgar A., Adjami M., Kazemi Nezhad M.H., (2016). Feasibility study on offshore wind farms in Persian Gulf and Oman Sea, and proposing optimal substructure and layout for assumed wind turbines and wind farms in the studied area. *Master Thesis in Khorramshahr University of Marine Sciences and Technology*.
- [5] Baroni M., Alali N., Bakhtiari M., Sadrinassab M (2016). Dynamic Response Analysis of Offshore Floating Wind Turbines. *Master Thesis in Shahrood University*.
- [6] Lackner, M. A., & Rotea, M. A. (2011). Structural control of floating wind turbines. *Mechatronics*, 21(4), 704-719.
- [7] Hu, Y., & He, E. (2017). Active structural control of a floating wind turbine with a stroke-limited hybrid mass damper. *Journal of Sound and Vibration*, 410, 447-472.
- [8] Colwell, S., & Basu, B. (2009). Tuned liquid column dampers in offshore wind turbines for structural control. *Engineering structures*, 31(2), 358-368.
- [9] Hokmabady, H., Mojtahedi, A., & Lotfollahi Yaghin, M. A. (2016). Structural Control and Fatigue Analysis of Offshore TLP Wind Turbine Using TMD. *Journal Of Marine Engineering*, 11(22), 39-50.
- [10] SACS manual, Fatigue, Release 6.
- [11] Zhao, X. L., Wilkinson, T. J., & Hancock, G. (2005). *Cold-formed tubular members and connections: Structural behaviour and design*. Elsevier.
- [12] American Petroleum Institute. Recommended Practice for Planning, Designing and Constructing Fixed Offshore Platforms-Working Stress Design, Twenty first edition, December 2000.



## Experimental evaluation of compressive, tensile strength and impact test in blast furnace slag based geopolymer concrete, under high temperature

Mohammadhossein Mansourghanaei <sup>a,\*</sup>, Morteza Biklaryan <sup>b</sup>

<sup>a,b</sup>Department of Civil Engineering, Chalous Branch, Islamic Azad University, Chalous, Iran

**Article History:** Received date 2022.08.31; revised date : 2022.08.11; accepted 2022.09.12

---

### Abstract

Today, the use of nanoscale additives in the concrete industry with the aim of reducing the negative effects of Portland cement and improving the mechanical properties of concrete has received much attention. Also, in order to reduce the harmful environmental effects and increase the mechanical properties and durability of concrete, particles with high pozzolanic properties are used as a suitable alternative to ordinary cement in concrete. In this regard, geopolymer concrete using materials containing aluminosilicate materials with adhesive properties and filler, as an alternative to cement, has attracted the attention of researchers. Concrete resistance to high heat is of particular importance. Geopolymer concrete has a good performance against heat due to its strong structure. In the current study, slag-based geopolymer concrete was used with 0-2% polyolefin fibers and 0-8% nano-silica to improve its structure. After curing the specimens under dry conditions at a temperature of 60°C in an oven, they were subjected to Compressive strength, Tensile strength, and Drop weight hammer tests to evaluate their mechanical properties. all tests were performed at 90 days of age under ambient temperature (20 °C) and high temperature (500 °C). The addition of nano-silica enhanced the whole properties of the slag-based geopolymer concrete. Addition of up to 8% nanosilica to the geopolymer concrete composition at 20% temperature improved the compressive strength test results up to 21.94%, tensile strength up to 15.19% and impact energy up to 36.36%. Addition of up to 2% of polyolefin fibers to the geopolymer concrete composition improved the tensile strength up to 11.76%, the impact energy up to 8.26 times and the compressive strength drop up to 22.49%. Applying high heat to geopolymer concrete samples reduced the compressive strength up to 16%, tensile strength up to 21% and impact energy up to 72.72%. The effect of heat on the drop in results in control concrete is more than geopolymer concrete. In the following, by conducting the SEM test, a microstructure investigation was carried out on the concrete samples. In addition to their overlapping with each other, the results indicate the geopolymer concrete superiority over the regular concrete. Besides, it demonstrated the positive influence of nano-silica addition on the concert microstructure. (DOI:<https://doi.org/10.52547/JCER.4.2.12>)

**Keywords :** Geopolymer Concrete; Polyolefin Fibers; Nano silica; Blast furnace slag; Scanning electron microscope (SEM).

---

\*Corresponding author. Tel.: +98 912 171 2070; E-mail: Mhm.ghanaei@iauc.ac.ir

## 1. Introduction

Cement production while consuming fossil fuels has many environmental hazards, in this regard, the production of concrete with cement alternative materials has always been the focus of researchers. Recently, the production of geopolymer concrete with high environmental properties and strength has been on the agenda of researchers. Research shows that cement plants are responsible for emitting about 5% of the total CO<sub>2</sub> into the Earth's atmosphere [1]. But The amount of CO<sub>2</sub> produced in the geopolymer process is much less than the cement production process [2]. Geopolymer is a name coined by Davidovits [3]. Geopolymer cements are a group of alkali-activated materials exhibiting superior engineering properties compared to Portland cements [4]. Geopolymer is characterized by high polymerization materials with aluminosilicate structure, which is mainly composed of three cross-linked unit dimensions, including (SiQ4 (2Al) and SiQ4 (3A) [5]. The activation of blast-furnace slag with alkaline liquids (e.g., NaOH or water glass) to produce alkali-activated slag cement has been studied during the past few decades [4]. Granulated Blast Furnace Slag (GBFS) is among the environmental materials. Using this material instead of cement can improve concrete resistance and decrease the increasing demand for its usage in concrete [6,7]. In addition to positively affecting the mechanical properties, the presence of silica particles in the geopolymer concrete accelerates the geopolymer reaction, reducing the compound alkalinity [8]. The influence of the nano-silica in improving the strength can be attributed to the following multi-stage mechanism that improves the concrete's microstructures and thus, increases the mechanical properties.

1. The rise in the pozzolanic reaction [8]. The presence of nano-silica in the geopolymer concrete accelerates the pozzolanic reaction.
2. The filling effect of nano-silica particles [9,10]. First, the distribution of nano-silica particles besides the other concrete particles results in a denser matrix. Second, the nano-silica's reaction in the geopolymerization procedure produces a larger amount of aluminosilicate gel, along with the reaction products of the main materials. The reaction

by-product is likely to deposit in the structure of the existing pores. The rise in SiO<sub>2</sub> increases the matrix density [11]. Therefore, the filling effect of Nano-silica is improved by the particle packing, and the by-product produces a denser matrix, reducing the porosity and increasing the strength.

3. It acts as a nucleus [12,13]. In the C-S-H gel structure, nanoparticles can act as a nucleus and form strong bonds with the C-S particles of the gel. Thus, during the hydration, the products' stability increases, and the durability and mechanical products are expected to improve.

According to the investigations, nano-silica addition to the geopolymer concrete enhances its compressive strength until the Silica to Aluminum (Si/Al) ratio reaches 2% in the mixture and further silica addition decreases the compressive strength due to agglomeration and non-uniform distribution [14]. also, An improvement is reported in the respective compressive strength using nano-silica particles in the geopolymer concrete compound [15]. On the other hand, The optimum compressive strength and tensile strength coefficient were obtained by adding 6% nano-silica [16].

The presence of materials containing aluminosilicate materials in the composition of geopolymer concrete due to its pozzolanic properties, while participating in the reactivity accelerates the geopolymerization process. They fill the concrete and strengthen the bond between the aggregates and the cement paste in the interfacial transition zones (ITZ). It is done weaker. The structure of nanosilica-containing slag geopolymer concrete can be evaluated in microstructural and macrostructural dimensions. The macrostructural dimension consists of large components visible to the naked eye, which is divided into two phases of aggregate and geopolymer cement paste, but in the dimension. Microstructure Most components must be viewed with an electron microscope. According to the studies, using macroplastic fibers for concrete improvement instead of metal mesh and fibers has captured researchers' attention; the concrete-related industries widely use polyolefin-based fibers [17]. The studies have indicated that adding polyolefin fibers to the concrete beams significantly assists the resistance after being cracked due to increasing the modulus of elasticity [18]. In an investigation conducted on the

effect of adding 0.5 of polyolefin fibers to the geopolymer concretes, it was observed that the compressive resistance of the samples declined by 12-15%. The samples containing fibers with 55 mm in length had undergone lower compressive strength more than those with 48 mm in length [19,20]. The addition of fibers reduces the compressive strength [21]. Comparing the concrete containing regular Portland cement with geopolymer concrete, McNulty [22] asserted that the geopolymer concretes have higher compressive strength. The comparison of the specimens with and without nano-silica showed a small number of fine cracks in the fracture, which slightly increased the impact resistance. The fibers were more effective than the nano-silica. Moreover, with the addition of polyolefin fibers to the geopolymer concrete, its failure became more flexible. This behavior was also observed for various kinds of fibers in other studies [23-25]. Geopolymer concretes resistance in encountering a significant level of heating treatment depends on its constituent chemical compounds and also the temperature and the way of curing [26]. This structure (related to the geopolymer concrete) has some merits compared to the regular concrete, e.g., it provides better resistance performance at higher temperatures [27].

The concrete resistance performance against heat is complicated. When being exposed to a high temperature, geopolymer concrete experiences a number of changes indicated based on their thermal ranges [28].

1. The removal of evaporative water at 100 °C
2. Calcium Silicate Hydrates hydration starts at 180 °C; as the temperature increases to 200 °C, the vapor pressure continuously elevates in the geopolymer structure.
3. The OH hydroxyl groups are evaporated at 500 °C. The dihydroxylation changes the Aluminosilicate structure, reducing the resistance level.
4. An intensely porous ceramic structure is formed at 800 °C.

The effect of nano-silica on improving and reducing heat resistance can be explained as a multi-step mechanism that improves the microstructure of concrete and, consequently, increases the mechanical properties of concrete.

1- Increase in pozzolanic reaction [8]: Presence of nano-silica in geopolymer concrete increases the rate of pozzolanic reaction.

2- Filler effect of Nano-silica particles [29,10]. In the first step, the distribution of the nano-silica particles besides other particles in concrete leads to the creation of a more compact matrix. Secondly, nano-silica reaction in the geopolymerization process produces a greater amount of Aluminosilicate gels and reaction products from main materials.

3- Acting as a nucleus [30,31] In the structure of C-S-H gel, nanoparticles can act as a nucleus and create strong bonds with particles of C-S-H gel.

In this laboratory research, the production of slag geopolymer concrete with optimal performance in compressive strength, tensile strength and impact hammer is introduced as an innovation. On the other hand, according to the study of others regarding the reduction of CO<sub>2</sub> emissions by the production of geopolymer concrete, this issue is also one of the objectives of this research.

## 2. Experimental program

### 2.1 Materials

In this experimental study, the Portland cement type II with a 2.35 gr/cm<sup>3</sup> of specific weight according to standard En 197-1 and the Blast Furnace Slag was used in powder form with the density of 2.45 gr/cm<sup>3</sup> according to ASTM C989/C989M standard. The chemical properties of these materials are indicated in Table 1. The nano-silica particles made up of 99.5% SiO<sub>2</sub> with an average diameter in the range of 15 to 25 nm were used. Crimped polyolefin fibers according to ASTM D7508/D7508M standard, 30 mm in length, were also used, whose physical properties are shown in Fig. 1. The used fine aggregates were natural clean sand with a fineness modulus of 2.95 and a density of 2.75 gr/cm<sup>3</sup>, and the coarse aggregates were crushed gravel with a maximum size of 19 mm and a density of 2.65 gr/cm<sup>3</sup> according to the requirements of the ASTM-C33. In this study, the geopolymer concrete curing has been performed at 60 °C according to the geopolymer concrete standards extracted from prestigious articles in this field.



Table 1  
Chemical compositions of materials

Component	Slag (%)	Portland cement type (%)
SiO <sub>2</sub> (%)	29.2	21.3
Al <sub>2</sub> O <sub>3</sub> (%)	19.4	4.7
Fe <sub>2</sub> O <sub>3</sub> (%)	5.8	4.3
CaO (%)	38.6	62.7
MgO (%)	2.8	2.1
SO <sub>3</sub> (%)	2.6	2
K <sub>2</sub> O (%)	0.1	0.65
Na <sub>2</sub> O (%)	0.2	0.18
TiO <sub>2</sub> (%)	0.6	-
Free Cao	-	1.12
Blaine (cm <sup>2</sup> /gr)	2200	3200
Loss on ignition (%)	0.3	1.84


Tensile Strength (N/mm <sup>2</sup> )	>500	
Length (mm)	30	
Diameter (mm)	0.8	
Elasticity Modulus (GPa)	>11	
Bulk Density (g/cm <sup>3</sup> )	2400	

Figure. 1. Physical properties of the polyolefin fibers

## 2.2 Mix design

For accurate investigation, six mixture designs were considered, according to ACI 211.1-89 standard. The first sample included a regular concrete containing Portland cement where the water to cement ratio has considered to be constantly 0.45. Five other samples include geopolymer concrete with different nano-silica and polyolefin fibers. The geopolymer concrete samples are generally categorized into two groups: the first group lacks polyolefin fibers with the nano-silica amount of 0-8%. The second group contains 8% of nano-silica, where the polyolefin fibers are used in these designs in the form of 1 and 2 percent. In order to achieve the same performance in each mixture design and obtain a slump of about 20 ±100 mm, we have used normal polycarboxylate-based superplasticizers. Besides, 202.5 kg/m<sup>3</sup> of the alkaline solution is used in this case. The used alkaline solution is a combination of NaOH and Na<sub>2</sub>SiO<sub>3</sub> with the weight ratio of 2.5,

utilized with the mixture specific weight of 1483 kg/m<sup>3</sup> and the concentration of 12 M. The conducted studies indicate that due to the significant level of C-S-H formation when utilizing Na<sub>2</sub>SiO<sub>3</sub>, using a combination of NaOH and Na<sub>2</sub>SiO<sub>3</sub> increases the compressive strength compared to single employment of CaOH [32]. The samples mixture design is indicated in Table 2.

Table 2  
Details of the mix designs

Mix ID	Cement	Slag	Water	Nano silica	Coarse aggregates (Kg/m <sup>3</sup> )	Fine aggregates	polyolefin fibers	Super plasticizer
1 GC-NS0P00	450	0	202.5	0	1000	761.13	0	6.75
2 GC-NS0P00	0	450	0	0	1000	816.10	0	6.75
3 GC-NS4P00	0	432	0	18	1000	767.42	0	7.8
4 GC-NS8P00	0	414	0	36	1000	718.75	0	8.3
5 GC-NS8P01	0	432	0	36	1000	672.78	24	8.6
6 GC-NS8P02	0	432	0	36	1000	646.28	48	9

## 2.3 Test methods

After fabricating the samples, for better curing and increasing the resistance properties, the samples were placed in an oven at 80 °C with a thermal rate of 4.4 °C/min for 48 h. After taking them out of the oven, the samples were kept for 90 days at an ambient temperature. After curing the samples and before performing the tests heating under standard ISO834, the samples were placed in an oven at 500 °C for 1 h. In the end, by opening the oven door, the samples reached the ambient temperature [33]. In the following, the required experiments were conducted on the concrete samples, according to the related standards. In this study, the compressive strength tests were performed on 10-cm<sup>3</sup> cubic specimens based on BS EN 12390. Furthermore, to determine the tensile strength of the cylindrical specimens (15 cm in diameter and 30 cm in length), the splitting tests were conducted based on ASTM C496. The concrete's resistance to dynamic loads (impacts) was measured using the drop weight hammer test according to the report by the ACI 544-2R committee. This test was conducted with repeating impacts on disks with a diameter of 15 cm and a height of 63.5 cm.

### 3. Results and discussion

#### 3.1 Results of the compressive strength test

The results of the compressive strength test of concrete samples at 20°C and 500°C temperature are shown in Figure 2. Figure 3 shows the concrete sample after the compressive strength test.

The minimum and maximum compressive strengths obtained from the samples of control concrete and geopolymer concrete after exposure to 500 ° C belong to OC-NS0PO0 and GC-NS8PO0 designs of 38.89 and 75.99 MPa, respectively. GC-NS8PO0 is approximately 95% warmer than OC-NS0PO0 design. Increasing the fibers in GC-NS8PO1 and GC-NS8PO2 mixing designs, compared to GC-NS8PO0 geopolymer concrete design, increases the heat resistance of the sample. Has not been. The maximum and minimum compressive strength of the 90-day samples after heating compared to the 90-day concrete samples at room temperature belong to OC-NS0PO0 design and GC-NS8PO0 design by 37% and 8%, respectively. The percentage of reduction in compressive strength (under high temperature), the effect of the properties of the base materials (slag and nanosilica) constituting the geopolymer concrete in the samples of geopolymer concrete are evident in the results of the diagram. In this regard, the highest and lowest percentages of reduction in compressive strength of concrete samples belong to the design of OC-NS0PO0 and GC-NS8PO2 by 37 and 8%, respectively.

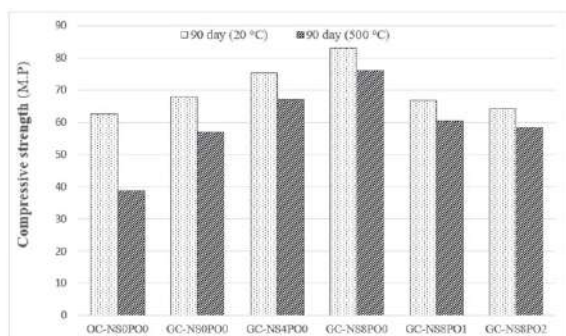


Figure 2. The compressive strength of the specimens



Figure 3. Concrete specimen after compressive strength test

#### 3.2 Results of the tensile strength test

The results of the tensile strength test of concrete samples at 20°C and 500°C temperature are shown in Figure 4. Figure 5 shows the concrete sample after the tensile strength test. Based on the results, it can be seen that the minimum and maximum tensile strengths obtained from the samples of control concrete and geopolymer concrete after heating at 500 ° C belong to the OC-NS0PO0 and GC-NS8PO2 designs of 2.47 and 4.73 MPa, respectively. The strength increase is approximately 91% for the GC-NS8PO2 design compared to the OC-NS0PO0 design. The sample was exposed to heat after the samples were exposed to heat. The maximum increase in strength belongs to the GC-NS8PO2 design by 36% compared to the GC-NS0PO0 design of geopolymer concrete. The maximum and minimum tensile strength of the 90-day samples after heating compared to the 90-day concrete samples at room temperature belong to OC-NS0PO0 design and GC-NS8PO1 design by 51% and 12%, respectively. In the diagram, the highest and lowest percentages of tensile strength reduction (under high temperature) of concrete samples belong to OC-NS0PO0 and GC-NS8PO1 designs by 51 and 12%, respectively.

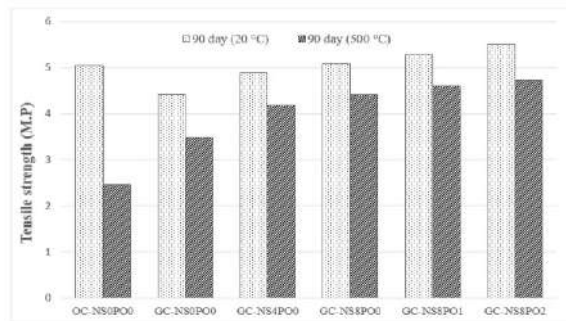


Figure 4. The tensile strength of the specimens



Figure 5. Concrete specimen after tensile strength test

### 3.3 Results of the impact test

The results of the impact test of concrete samples at 20°C and 500°C temperature are shown in Figure 6. Figure 7 shows the concrete sample after the impact test. Following the results, it is observed that with increasing heat in control concrete samples, the resistance of the samples to falling hammer blows decreases and the absorbed energy (6 times) and refractive energy (5 times) of concrete samples also decreases. Addition of 8% nanosilica and 2% polyolefin fibers to the composition of geopolymer concrete has improved the results of fracture energy and energy absorbed in the impact hammer test, this is due to the role of adhesion, filler and nucleation of

silica nanoparticles in mortar Geopolymer cement and end products of geopolymerization. The amount of adsorption energy by adding 1 and 2% of fibers increases the absorbed energy by 6.2 and 9.3 times, respectively, which indicates the good ability of fibers to absorb impact energy. At 20 ° C, the minimum (223.89 J) and maximum (2829.15 J) energy absorbed in concrete samples belong to the GC-NS0PO2 and GC-NS8PO2 designs, respectively. At 500 ° C, the minimum (40.71 J) and maximum (773.44 J) absorbed energies of the OC-NS0PO0 and GC-NS0PO2 designs were obtained, respectively.

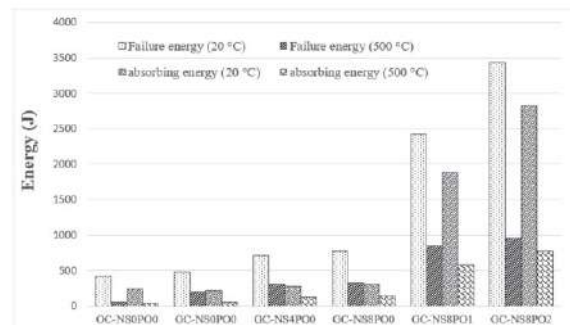


Figure 6. The impact of the specimens



Figure 7. Concrete specimen after impact strength test

### 3.4 Results of the SEM test

In this study, 10 μm scale scanning electron microscopy images at 90 days of curing age are shown on concrete samples at room temperature in Figure 8 and under high temperature in Figure 9.

In the samples under room temperature, for geopolymer concrete, by increasing the consumption of nanosilica in the designs and due to the acceleration and greater participation of these particles in the geopolymerization process, we see an

increase in the production of hydrated gels in geopolymer concrete samples. In these images, the amount of white masses due to non-participation of particles in the chemical reaction process in Figure 1 (including control concrete containing Portland cement) is higher than other designs (including ferrous concrete). The increase in the volume of masses obtained from hydrated gels in the geopolymerization product is evident by increasing the amount of nanosilica in alkaline concrete designs. The reduction of porosity in the concrete microstructure has been reduced. In Portland cement, C-S-H gel consists of silicone and geopolymer groups of materials with high polymerization and Aluminosilicate structure [34]. In the sample containing nano-silica, very few fine cracks are observed, in which nano-silica acts as a filler to fill the spaces inside the hardened microstructure skeleton of the geopolymer paste and increase its compaction [14,35]. First, the nanoparticles fill the pores of the matrices, which reduces the porosity of the geopolymer nanocomposites, resulting in uniformity, less pores, and a more compact geopolymer matrix [8]. In fact, the pozzolanic reaction condenses and homogenizes the microstructures by converting C-H to C-S-H [5], thus creating more geopolymer gel and a denser matrix [36]. However, further increase in NS content causes insufficient dispersion and accumulation of nano-silica particles, which slightly reduces matrix density [34]. In high temperature samples, tree structure due to water evaporation and destruction of concrete microstructure is observed. In this case, cracks and cavities in the concrete microstructure are seen more than concrete samples under room temperature. High heat on concrete has caused fundamental changes in the microstructure of concrete and Portland cement paste matrix and geopolymer, this is one of the main factors reducing the mechanical properties of concrete under high temperature, heat causes water to escape in the capillary spaces between gels Hydrate in the interfacial transition areas in concrete, water outlet also causes pores and weakens the microstructure of concrete. In general, it is believed that due to their ceramic-like properties, geopolymers have better performance in encountering fire compared to regular concretes [8,37,38]. Geopolymer concretes resistance

in encountering a significant level of heating treatment depends on its constituent chemical compounds and also the temperature and the way of curing [26]. The OH hydroxyl groups are evaporated at 500 °C. The dihydroxylation changes the Aluminosilicate structure, reducing the resistance level [33]. According to the obtained results in this investigation, all designs at room temperature have "superior" quality, and all samples at 500°C have average and good quality [39].

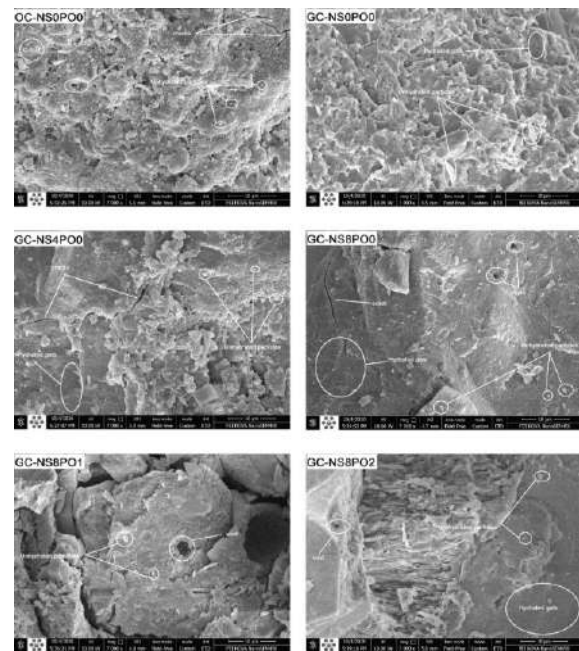


Figure. 8. Microstructure (SEM) image under room temperature



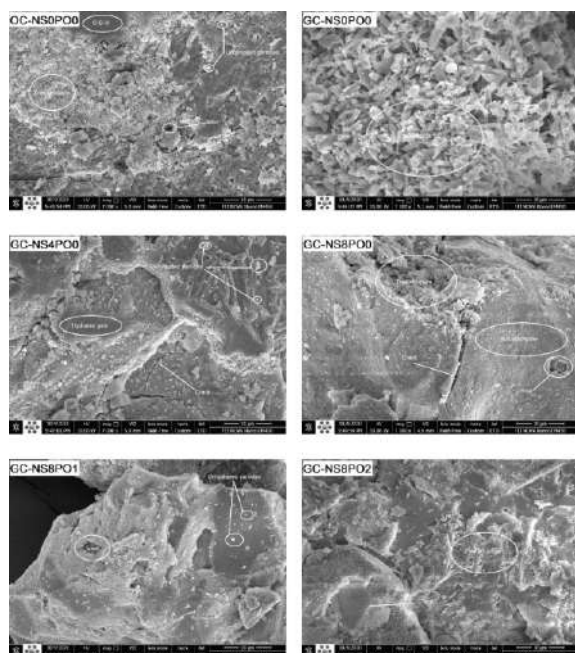


Figure. 9. Microstructure (SEM) image under high temperature

#### 4. Conclusions

In this experimental study, compressive strength, tensile strength and impact resistance of hammer dropping in ordinary concrete and geopolymer concrete at 90 days of curing age at 20% and 500% were investigated. The results of this research are as follows.

1. At a temperature of 20%, the lowest (62.43 M.P) and the highest (82.96 M.P) compressive strength belong to design concrete 1 (including ordinary concrete) and design 4 (including geopolymer concrete containing 8% nanosilica). The lowest (4.41 M.P) and the highest (5.51 M.P) tensile strength belong to Scheme 2 (including nanosilica-free geopolymer concrete) and Scheme 6 (including geopolymer concrete containing 2% fibers). The lowest (232.89 G) and highest (2829.15 G) impact energy in the falling hammer test belongs to Figure 2 and Figure 6.
2. At a temperature of 500%, the lowest (38.89 M.P) and the highest (75.99 M.P) compressive strength belong to design concrete 1 (including ordinary concrete) and design 4 (including geopolymer

concrete containing 8% nanosilica). The lowest (2.47 M.P) and the highest (4.73 M.P) tensile strength belong to design 1 and design 6 (including geopolymer concrete containing 2% fibers). The lowest (40.71 G) and highest (772.44 G) impact energy in the falling hammer test belongs to Figure 2 and Figure 6.

3. Applying high heat to geopolymer concrete samples reduced the compressive strength up to 16%, tensile strength up to 21% and impact energy up to 72.72%. The effect of heat on the drop in results in control concrete is more than geopolymer concrete.

4. The results of all tests at 20% and 500% showed the superiority of mechanical properties in geopolymer concrete compared to ordinary concrete.

5. SEM images, due to the microstructural superiority of geopolymer concrete over control concrete, covered the results of other tests in this study.

#### CRediT authorship contribution statement

##### Mohammadhossein Mansourghanaei:

Conceptualization, Methodology, Validation, Formal analysis, Investigation, Resources, Data curation, Writing - original draft, Writing - review & editing, Visualization, Supervision.

##### Morteza Biklaryan:

Conceptualization, Formal analysis, Resources, Data curation, Writing - original draft, Writing - review & editing, Visualization, Supervision.

#### Declaration of Competing Interest

The authors declare that they have no known competing financial interests or personal relationships that could have appeared to influence the work reported in this paper.

#### Acknowledgments

This research was done with the support of Islamic Azad University, Chalous Branch.

## References

- [1] Nosrati, A., Zandi, Y., Shariati, M., Khademi, K., Aliabad, M., Marto, A., & Khorami, M. (2018). Portland cement structure and its major oxides and fineness. *Smart structures and systems*, 22(2), 425-432.
- [2] Neupane, N., Chalmers, D., & Kidd, P. (2018). High-strength geopolymer concrete properties. advantages and challenges. *Advances in Materials*, 7(2), 15-25.
- [3] Davidovits J. Soft mineralogy and geopolymers. *Proc. 1st Int. Conf. on geopolymers*. 1988. p. 19-21.
- [4] Allahverdi, A. L. I., Ebrahim Najafi Kani, and Mahshad Yazdanipour. "Effects of blast-furnace slag on natural pozzolan-based geopolymer cement." *Ceramics-Silikáty* 55.1 (2011): 68-78.
- [5] Du, H., S. Du, and X. Liu, Durability performances of concrete with nano-silica. *Construction and building materials*, 2014. 73: p. 705-712.
- [6] Siddique, R. and D. Kaur, Properties of concrete containing ground granulated blast furnace slag (GGBFS) at elevated temperatures. *Journal of Advanced Research*, 2012. 3(1): p. 45-51.
- [7] Yüksel, İ., R. Siddique, and Ö. Özkan, Influence of high temperature on the properties of concretes made with industrial by-products as fine aggregate replacement. *Construction and building materials*, 2011. 25(2): p. 967-972.
- [8] Assaedi, H., et al., Influence of nano silica particles on durability of flax fabric reinforced geopolymer composites. *Materials*, 2019. 12(9): p. 1459.
- [9] Beigi, M.H., et al., An experimental survey on combined effects of fibers and nanosilica on the mechanical, rheological, and durability properties of self-compacting concrete. *Materials & Design*, 2013. 50: p. 1019-1029.
- [10] Deb, P.S., P.K. Sarker, and S. Barbhuiya, Sorptivity and acid resistance of ambient-cured geopolymer mortars containing nano-silica. *Cement and Concrete Composites*, 2016. 72: p. 235-245.
- [11] Law, D.W., et al., Long term durability properties of class F fly ash geopolymer concrete. *Materials and Structures*, 2015. 48(3): p. 721-731.
- [12] Bahadori, H. and P. Hosseini, Reduction of cement consumption by the aid of silica nano-particles (investigation on concrete properties). *Journal of Civil Engineering and Management*, 2012. 18(3): p. 416-425.
- [13] Bosiljkov, V.B., SCC mixes with poorly graded aggregate and high volume of limestone filler. *Cement and Concrete Research*, 2003. 33(9): p. 1279-1286.
- [14] Deb, P.S., P.K. Sarker, and S. Barbhuiya, Effects of nano-silica on the strength development of geopolymer cured at room temperature. *Construction and building materials*, 2015. 101: p. 675-683.
- [15] Adak, D., M. Sarkar, and S. Mandal, Structural performance of nano-silica modified fly-ash based geopolymer concrete. *Construction and Building Materials*, 2017. 135: p. 430-439.
- [16] Adak, D., M. Sarkar, and S. Mandal, Effect of nano-silica on strength and durability of fly ash based geopolymer mortar. *Construction and Building Materials*, 2014. 70: p. 453-459.
- [17] Alberti, M.G., A. Enfedaque, and J.C. Gálvez, Improving the reinforcement of polyolefin fiber reinforced concrete for infrastructure applications. *Fibers*, 2015. 3(4): p. 504-522.
- [18] Chellapandian, M., A. Mani, and S.S. Prakash, Effect of macro-synthetic structural fibers on the flexural behavior of concrete beams reinforced with different ratios of GFRP bars. *Composite Structures*, 2020. 254: p. 112790.
- [19] Noushini, A., A. Castel, and R.I. Gilbert, Creep and shrinkage of synthetic fibre-reinforced geopolymer concrete. *Magazine of Concrete Research*, 2019. 71(20): p. 1070-1082.
- [20] Noushini, A., et al., Mechanical and flexural performance of synthetic fibre reinforced geopolymer concrete. *Construction and Building Materials*, 2018. 186: p. 454-475.
- [21] Galan, A. Estimate of concrete strength by ultrasonic pulse velocity and damping constant. in *Journal Proceedings*. 1967.
- [22] McNulty, E., Geopolymers: an environmental alternative to carbon dioxide producing ordinary Portland cement. Department of Chemistry, The Catholic University of America, 2009.
- [23] Alberti, M.G., A. Enfedaque, and J.C. Gálvez, Improving the reinforcement of polyolefin fiber reinforced concrete for infrastructure applications. *Fibers*, 2015. 3(4): p. 504-522.
- [24] Olivito, R. and F. Zuccarello, An experimental study on the tensile strength of steel fiber reinforced concrete. *Composites Part B: Engineering*, 2010. 41(3): p. 246-255.
- [25] Islam, A., et al., Influence of steel fibers on the mechanical properties and impact resistance of lightweight geopolymer concrete. *Construction and Building Materials*, 2017. 152: p. 964-977.
- [26] Türkmen, İ., et al. Fire resistance of geopolymer concrete produced from Ferrochrome slag by alkali

- activation method. in 2013 International Conference on Renewable Energy Research and Applications (ICRERA). 2013. IEEE.
- [27] Aslani, F., Thermal performance modeling of geopolymer concrete. *Journal of Materials in Civil Engineering*, 2016. 28(1): p. 04015062.
- [28] Bakhtiyari, S., et al., Self-compacting concrete containing different powders at elevated temperatures– Mechanical properties and changes in the phase composition of the paste. *Thermochimica acta*, 2011. 514(1-2): p. 74-81.
- [29] Beigi, M.H., et al., An experimental survey on combined effects of fibers and nanosilica on the mechanical, rheological, and durability properties of self-compacting concrete. *Materials & Design*, 2013. 50: p. 1019-1029.
- [30] Bahadori, H. and P. Hosseini, Reduction of cement consumption by the aid of silica nano-particles (investigation on concrete properties). *Journal of Civil Engineering and Management*, 2012. 18(3): p. 416-425.
- [31] Bosiljkov, V.B., SCC mixes with poorly graded aggregate and high volume of limestone filler. *Cement and Concrete Research*, 2003. 33(9): p. 1279-1286.
- [32] Pilehvar, S., et al., *Physical and mechanical properties of fly ash and slag geopolymer concrete containing different types of micro-encapsulated phase change materials*. *Construction and Building Materials*, 2018. 173: p. 28-39.
- [33] Kong, D.L. and J.G. Sanjayan, *Effect of elevated temperatures on geopolymer paste, mortar and concrete*. *Cement and concrete research*, 2010. 40(2): p. 334-339.
- [34] Supit, S.W.M. and F.U.A. Shaikh, Durability properties of high volume fly ash concrete containing nano-silica. *Materials and structures*, 2015. 48(8): p. 2431-2445.
- [35] Shih, J.-Y., T.-P. Chang, and T.-C. Hsiao, Effect of nanosilica on characterization of Portland cement composite. *Materials Science and Engineering: A*, 2006. 424(1-2): p. 266-274.
- [36] Phoo-ngernkham, T., et al., The effect of adding nano-SiO<sub>2</sub> and nano-Al<sub>2</sub>O<sub>3</sub> on properties of high calcium fly ash geopolymer cured at ambient temperature. *Materials & Design*, 2014. 55: p. 58-65.
- [37] Ryu, G.S., et al., The mechanical properties of fly ash-based geopolymer concrete with alkaline activators. *Construction and Building Materials*, 2013. 47: p. 409-418.
- [38] Mehdipour, S., et al., Mechanical properties, durability and environmental evaluation of rubberized concrete incorporating steel fiber and metakaolin at elevated temperatures. *Journal of Cleaner Production*, 2020. 254: p. 120126.
- [39] Whitehurst, E.A. Soniscope tests concrete structures. in *Journal Proceedings*. 1951.



## Study on the Performance of High-Strength Steel Shear Wall with Opening and Pre-crack

Mohammad komeil Sadeghi golafshani <sup>a,\*</sup>

<sup>a</sup>Department of Civil Engineering, Chalous Branch, Islamic Azad University, Chalous, Iran

**Article History:** Received date 2022.08.31; revised date : 2022.08.11; accepted 2022.09.12

---

### Abstract

The use of steel shear wall in engineering construction, including high-rise building projects that bear high lateral forces, is of great importance and practical. Since the steel shear wall with opening may have some pre-cracks due to initial damage and cause the weak lateral behavior of the shear wall, in this study, the simultaneous impact of pre-crack and opening in the three-story and one-span frame with steel shear wall has been evaluated. In this study, 48 numerical samples have been studied using the finite element method and Abaqus software. Axial and lateral loading has been applied to the samples, and the parameters of the pre-crack position, pre-crack length and the type of shear wall steel sheet material have been investigated. The results of this study demonstrated that the numerical model made for the shear wall provides reliable answers compared to the laboratory model. In the shear walls under study, the parameter of crack length and crack position has a high impact on the ductility capacity, while it has little impact on the hardness and strength index. The most critical pre-crack modes in the horizontal position, located at the top or bottom corner of the frame, have had a great impact on the lateral behavior and reduced ductility by 60% and wall strength by 32%. On the other hand, by changing the materials of the shear wall steel sheet from LYP steel to St37 and St52, the final strength and hardness have increased by 3.63 and 1.45 times, respectively and the ductility has decreased by 30%. (DOI:<https://doi.org/10.52547/JCER.4.2.22>)

**Keywords:** steel shear wall, circular opening, horizontal and vertical pre-crack, axial-lateral loading, finite performance

---

\* Corresponding author. Tel.: +98 912 021 2987; E-mail: mk.sadeghi92@gmail.com



## 1. Introduction

The steel plate shear wall (SPSW) system is a type of lateral force resisting structure that consists of filling plates and boundary elements. SPSWs offer quick installation and easy production standardization. In a study, Thorburn [1] showed that a thin steel plate after buckling forms a tensile field that can continue to resist horizontal load. The postbuckling performance of thin SPSWs has attracted the attention of researchers. In another study, Elgaaly [2] and Caccese [3] found that out-of-plane buckling occurs in thin SPSW under a small shear load and a "pinching" phenomenon appears in the hysteresis curve. In general, stiffeners are placed to steel plates in order to improve their performance. The common shapes of stiffeners in common shear walls with openings include cross stiffeners, diagonal stiffeners, multiple stiffeners, etc. [4,5] which have been evaluated in previous studies. Chen [6] investigated the elastic buckling behavior and hysteresis behavior of stiffened SPSWs. The results indicate that the elastic buckling load is linearly related to the bending stiffness of diagonal stiffeners that diagonally have been reinforced with stiffeners and SPSWs and have better bearing capacity and hysteresis performance than SPSWs with cross stiffeners. Guo [7] in a different research showed that semi-rigid connections weaken the overall stability of the structure and change the distribution of forces and bending moments of the connections. Sigariyazd [8] conducted one-way static pushover tests on a diagonally stiffened SPSW and a slanted stiffener SPSW, studied the effect of slanted stiffeners on the bearing capacity, and presented a theoretical formula for calculating the bearing capacity.

In another study, Alavi [9,10] suggested that a channel-shaped stiffener with high torsional stiffness can be used as a more effective stiffener. Du [11] and Deng [12] used a multi-crenation network of channels and a diagonal channel to repair damaged SPSW. Channel stiffeners effectively repaired the damaged plate and reduced the tension field effect. Tong [13] investigated the elastic buckling behavior of trapezoidal-corrugated SPSW with vertical stiffener. Xu [14] and Tong [15] proposed stiffness formulas for vertical channel stiffened plate under shear or compression loading.

In a study, Nie [16] tested SPSWs with a vertical channel stiffener having openings. The results show

that the opening can reduce the stiffness and bearing capacity of the structure, and by placing the stiffener at the edge of the opening, the stability of the structure increases. Hosseinzadeh [17] conducted a nonlinear numerical analysis of a SPSW with large rectangular openings and stiffeners. In various stiffened perforated structures, the stiffened open edge can increase both ultimate strength and stiffness while slightly reducing the ductility ratio. Sabouri Ghomi [18] evaluated the impact of two openings on the structural behavior of SPSWs. Opening distance had little effect on lateral bearing capacity, stiffness and energy absorption. However, the opening caused the depression of these numbers. Shekastehband [19] studied the seismic behavior of a SPSW with fully connected John plates and only beams. The ductility ratio of the structure can be improved only when connected to beams, but the energy dissipation capacity and shear strength of the structure are clearly lower than those of fully connected John plates. To study the effect of different opening shapes and hardening shapes on the hysteresis behavior of SPSWs, two samples with a scale of 1 to 3 were designed. A sample was reinforced SPSW with a diagonal channel and two rectangular openings. The other was a stiffened SPSW inclined channel with a rectangular opening.

Since steel panels can have considerable strength and stiffness, they may sometimes impose a greater share of floor shears on boundary columns, which may lead to their premature failure. Attempts to reduce the columns demand in SPSWs have recently been made using cold-rolled steel panels, [20] the use of LYP steel plates, [21-22] the use of perforated John plates with regular circular holes [23] and the use of semi-supported steel shear walls (SSSWs) [24-25] have been proposed. Shekastehband et al. [26] studied the effects of hole diameter as well as slenderness ratios of John plates on the seismic behavior of SSSWs. Based on the test results, the strength, stiffness, ductility coefficient and energy absorption characteristics of the samples were significantly reduced in the samples with openings. Wei et al. [27] investigated a series of new semi-connected SPSWs. The results of the proposed test showed that the proposed SPSW demonstrates good structural performance in terms of initial stiffness, shear strength, ductility, and energy absorption capability. In this article, 48 samples of steel frames with circular openings and pre-cracks have been simulated

using the finite element method and quasi-static analysis. Bearing capacity, pushover behavior, ductility, damage of the samples are presented.

## 2. Finite Element Method

Laboratory studies are the most effective method for research in the field of structural behavior which becomes important due to the expensive and time-consuming nature of numerical studies. Many studies have been conducted in the field of steel shear wall. The results of using the numerical method for these studies show that the ABAQUS [28] software has a good performance in the responses of non-linear behavior of materials and hysteresis diagrams. In order to study more on the behavior of unstiffened thin steel shear wall structures, an efficient and accurate finite element method should be proposed. The steel sheet shear wall structure consists of beams, columns, steel filler panel and connection plates. Past studies proved that residual stress has little effect on the shear wall behavior of steel sheet, which can be neglected in the modeling process. Beam, column and steel panel are created in ABAQUS with shell elements (S4R). Initial out-of-plane defects should be considered. In the modeling process, the buckling modes are calculated to extract the lowest buckling mode. Then, the "defect" command is used to modify the coordinates of the panel nodes based on buckling and the maximum out-of-plane deformation value is multiplied by it.

Boundary conditions and out-of-plane supports and constraints are considered similar to laboratory works [29]. The loading pattern consists of two stages: vertical loads and incremental lateral displacements. Cyclic structural model (composite hardening) is adopted to accurately simulate the behavior of steel, using ABAQUS material library of nonlinear kinematic hardening software. This model is parameterized in ABAQUS (Hardening = COMBINED model). Since the analysis of the thin steel plate shear wall under lateral loadings has severe nonlinear behaviors, including panel buckling, local column buckling, large out-of-plane deformation, and bidirectional tensile bands, the analyzes were performed with the nonlinear static module.

## 3. Research method

Steel shear wall with opening and pre-crack is evaluated in the present article in two parts. Since the

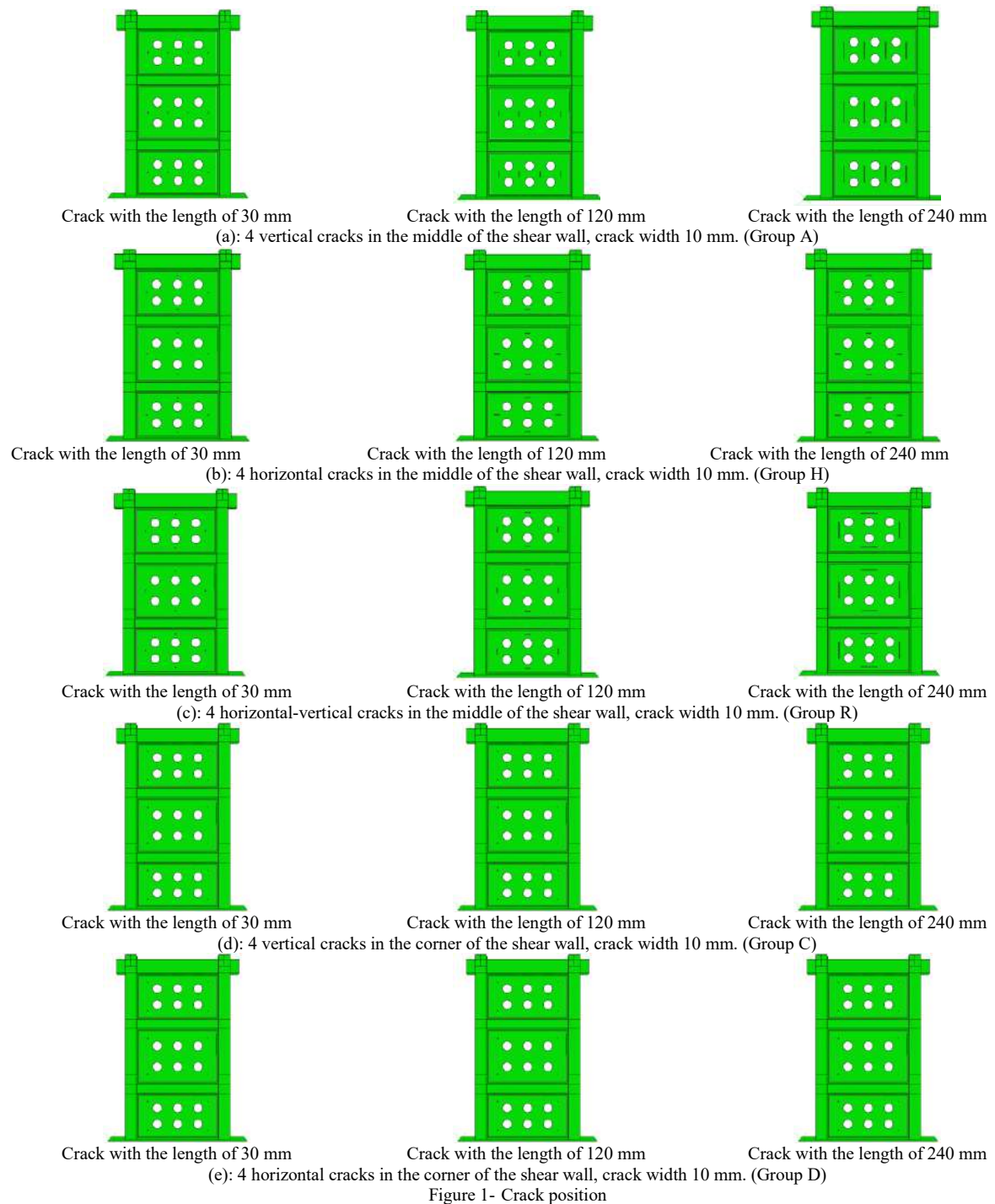
finite element analysis of shear wall with opening and three-story frame is complicated and there is high probability of cracking, a numerical model is proposed to estimate the force-displacement response of SPSW. Using the presented idea, in the first step, cracks with a width of 10 mm and different lengths were created in the steel shear wall, and then in the second step, the push-over curve was obtained using the finite element method. There are various positions and combinations for cracking, which are shown below. As shown in Figure 4, this type of crack includes horizontal and vertical cracks in different positions of the steel frame filler plate. Critical cracks may occur in any position on the wall despite the openings, for this purpose, the composite of the position of more cracks in the tensile and compress field is considered.

## 4. Validation

In order to control and validate the behavior of the constructed finite element model, it is necessary to make a comparison between the results of the analytical and the laboratory model. The present study was conducted by numerical simulation using ABAQUS finite element simulator software. This comparison was made between the responses obtained from ABAQUS finite element modeling and Zhang et al.'s laboratory research [29].

In this article, a TM1 model, a three-story frame and a one-span steel shear wall presented by Zhang et al. is simulated with a center-to-center height of 2.05 m and a thickness of 6 mm steel filler plate and different cross-sections of column beams as shown in Figure 2. The boundary members are made of ASTM-A572 steel, which is considered as a Tie constraint in welding modeling, and the filler sheet is made of steel with a yield point of 235 MPa. The schematic of the frame is shown in Figure 2. The type of element for steel shear wall modeling in ABAQUS finite element software is shell element.

The element used in boundary members (beam, column and support) and stiffeners and filler sheet, which is collectively called shear wall, is of S4R type. In order to achieve the appropriate mesh size, different dimensions have been selected for the



elements, and by comparing and calibrating the numerical and laboratory results, the mesh size of 25 mm has been selected for the numerical samples, which has brought acceptable results.

The laboratory model of the shear wall investigated by Zhang et al. is shown in Figure 2 and the compared force-displacement diagram obtained from the laboratory results and modeling in ABAQUS software is shown in Figure 3. Figure 3 shows the force-displacement diagram obtained from the laboratory and the simulation results obtained from the finite element software, which has a slight difference with the laboratory results and is in good agreement with the laboratory results of Zhang et al. This comparison demonstrates the accuracy of the answers obtained from ABAQUS in the research and the accuracy of this software in modeling.

### 5. Parametric Study

In this study, steel shear walls with opening and pre-crack have been analyzed for axial and lateral compressive load. This study aims at investigating the lateral behavior of the shear wall of thin steel plate with pre-crack under lateral horizontal forces and at calculating the stiffness index, ultimate strength and ductility. The objective of the study is the shear panel with opening and pre-crack, on which the tensile fields of the adjacent panels above and below are applied. According to the applied engineering experience and published research, the selected size range of the thin steel sheet shear wall is as follows: the ratio of opening to height is about  $L/h = 1.5-2.0$  and the ratio of height to thickness is about  $\lambda = 200-400$ . Based on these principles, 5 groups of pre-cracks were made in the three-story non-stiffened steel sheet shear wall sample. The steel sheet shear wall structure is generally composed of edge beams, edge columns, filler panels, beam-to-column connections, and opening plates. Welded steel frame is used as boundary members. The width of the plates connecting the shear sheet to the boundary members is 60 mm and its thickness is 8 mm. The capacity of the panels is calculated and designed by CAN/CSA-S16-01 and ANSI/AISC 341-05 standards.

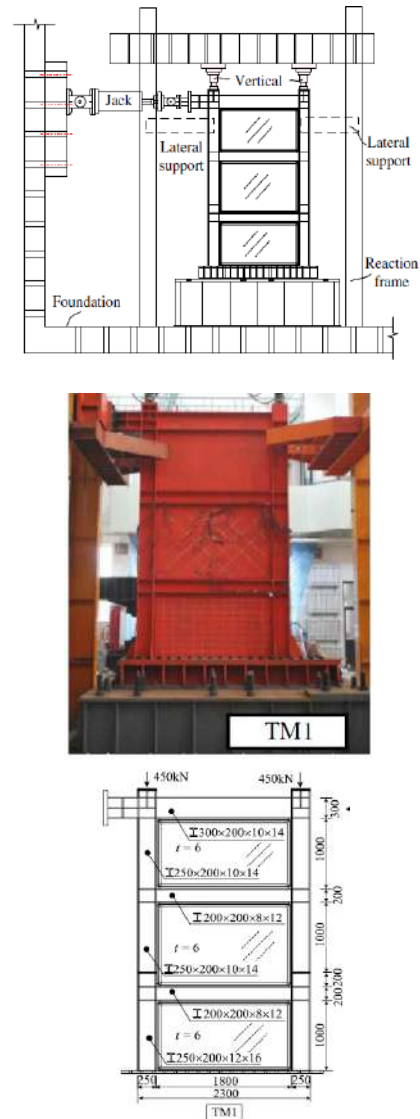


Figure 2 - Shear wall modeling in Zhang et al.'s research

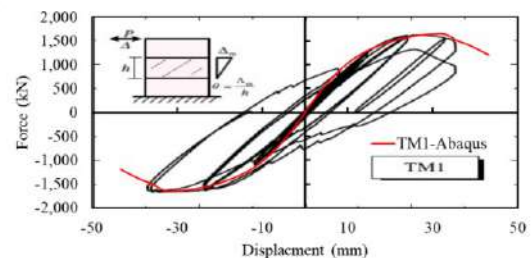


Figure 3 - Comparing the results of the force-displacement diagram in Zhang et al.'s research and ABAQUS

Also,  $h_s$  is the central distance between the edge beams,  $I_c$  the bending stiffness of the edge column,  $L_s$  the central distance between the edge columns,  $A_c$  the area of the column,  $A_b$  the area of the beam and  $h$  the height of the panel.

$$\tan^4 \alpha = \frac{1 + \frac{L_s t_l}{2 A_c}}{1 + \frac{h_s t_l}{A_b} + \frac{h_s^4 t_l}{360 I_c L_s}} \quad M_u = (f_{py} t_l h_s^2 \sin^2 \alpha) / 12$$

$$V_u = 0.25 f_{py} t_l h_s \sin^2 2\alpha$$

In the field of stiffness index, an approximate estimate has been reported in previous research, which used the initial slope of the force-displacement diagram and was used to calculate the ultimate strength and ductility indices from the maximum force and the ratio of the ultimate displacement to the yield displacement. In what follows, a detailed parametric study has been conducted to evaluate the pushover behavior of steel shear wall with pre-crack, for the parameters of pre-crack position, pre-crack length and the type of steel panel material. For the crack position parameter in group A, 4 vertical cracks in the middle of the shear wall, in group H 4 horizontal cracks in the middle of the shear wall, in group R 4 horizontal-vertical cracks in the middle of the shear wall, in group C 4 vertical cracks in the corner of the shear wall and in group D, 4 horizontal cracks in the corner of the shear wall are considered and the crack width is 10 mm in all models. For the crack length parameter, 30, 120 and 240 mm and for the material parameter of the steel panel LYP100, St37 and St52 are considered. The details of the numerical samples for the 48 studied frames are presented in Table 1.

## 6. Force-displacement Curves

In this part, the push-over behavior of pre-cracked steel shear wall with circular openings is compared. All the features of the steel frame and plate are similar for all samples. All samples were subjected to 3% circulation. The behavior of steel shear wall with circular openings in two rows of shear wall was considered. All models are divided into 3 groups, the first group is related to the position of the pre-crack, the second group to the length of the pre-crack, and the third group to the steel material of the filler sheet of the steel frame. The force-displacement diagrams

for different modes of the parametric study are shown in Figures 4 to 6.

First, vertical loads were applied to the numerical specimens until the loads reached 500 kN. Using buckling analysis and the shape data of the first mode of the wall, small deformations outside the wall with a value of  $L/1500$  were applied. No out-of-plane deformation was revealed in the specimens under examination until the time before yielding. With the increase in the lateral load, when the first elements reached the yield stress, out-of-plane deformation and buckling were observed around the cracks, and stress concentration was seen in the tensile bands and around the cracks. As the loading displacement increased, out-of-plane deformations and cross tensile bands were more and more evident. The filler panel entered the plastic stage earlier than the boundary members, which has fulfilled the principle of "strong frame and weak panel". During the period of below 1%, there is no buckling phenomenon. When the shear wall frame load reached  $3\Delta y$ , instability and overall buckling occurred. This phenomenon was caused by the presence of pre-cracks and openings in the steel plate filling the frame. In the following, the effect of the parametric study on the lateral behavior and indices of the shear steel frame has been investigated.

### 6-1. The Impact of the Pre-break Position Parameter

In this part, the impact of the crack position on the lateral behavior of the shear wall has been investigated. In the figure, 9 curves are drawn, in each curve 5 graphs are drawn for 5 different modes of the pre-crack position. Numerical models, stiffness, ultimate strength and ductility indices have been compared. For modes of steel shear wall that has a 30 mm crack and different steel materials, the crack position parameter has no impact on the stiffness, ultimate strength, and ductility indices in each group, and the values of the indices and their percentage changes are given in Table 2. By changing the position of the crack in modes of steel shear wall that has a crack of 120 and 240 mm, the change in the position of the crack is more tangible.

The reduction of stiffness indices for the shear wall with different cracks and with LYP material has been achieved in the range of 14 to 22%, the ultimate strength index with the decreasing range of 8 to 15%, and the ductility with a decreasing trend of 12 to

Table 1. details of the numerical samples

No.	Name of shear wall	Crack position	Crack length(mm)	Type of steel	No.	Name of shear wall	Crack position	Crack length(mm)	Type of steel
1	DSW-N-0-LYP	-	0	LYP	25	DSW-R-120-ST37	R	120	ST37
2	DSW-A-30-LYP	A	30	LYP	26	DSW-R-240-ST37	R	240	ST37
3	DSW-A-120-LYP	A	120	LYP	27	DSW-C-30-ST37	C	30	ST37
4	DSW-A-240-LYP	A	240	LYP	28	DSW-C-120-ST37	C	120	ST37
5	DSW-H-30-LYP	H	30	LYP	29	DSW-C-240-ST37	C	240	ST37
6	DSW-H-120-LYP	H	120	LYP	30	DSW-D-30-ST37	D	30	ST37
7	DSW-H-240-LYP	H	240	LYP	31	DSW-D-120-ST37	D	120	ST37
8	DSW-R-30-LYP	R	30	LYP	32	DSW-D-240-ST37	D	240	ST37
9	DSW-R-120-LYP	R	120	LYP	33	DSW-N-0-ST52	-	0	ST52
10	DSW-R-240-LYP	R	240	LYP	34	DSW-A-30-ST52	A	30	ST52
11	DSW-C-30-LYP	C	30	LYP	35	DSW-A-120-ST52	A	120	ST52
12	DSW-C-120-LYP	C	120	LYP	36	DSW-A-240-ST52	A	240	ST52
13	DSW-C-240-LYP	C	240	LYP	37	DSW-H-30-ST52	H	30	ST52
14	DSW-D-30-LYP	D	30	LYP	38	DSW-H-120-ST52	H	120	ST52
15	DSW-D-120-LYP	D	120	LYP	39	DSW-H-240-ST52	H	240	ST52
16	DSW-D-240-LYP	D	240	LYP	40	DSW-R-30-ST52	R	30	ST52
17	DSW-N-0-ST37	-	0	ST37	41	DSW-R-120-ST52	R	120	ST52
18	DSW-A-30-ST37	A	30	ST37	42	DSW-R-240-ST52	R	240	ST52
19	DSW-A-120-ST37	A	120	ST37	43	DSW-C-30-ST52	C	30	ST52
20	DSW-A-240-ST37	A	240	ST37	44	DSW-C-120-ST52	C	120	ST52
21	DSW-H-30-ST37	H	30	ST37	45	DSW-C-240-ST52	C	240	ST52
22	DSW-H-120-ST37	H	120	ST37	46	DSW-D-30-ST52	D	30	ST52
23	DSW-H-240-ST37	H	240	ST37	47	DSW-D-120-ST52	D	120	ST52
24	DSW-R-30-ST37	R	30	ST37	48	DSW-D-240-ST52	D	240	ST52

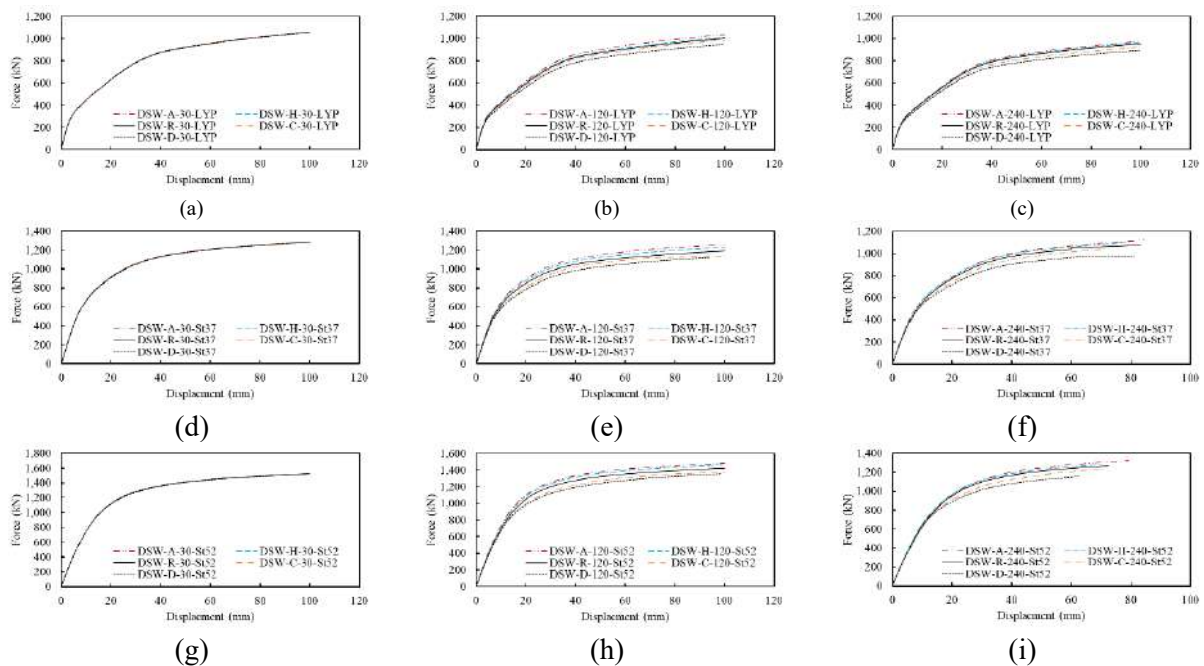


Figure 4 – Comparison of force-displacement curves for the pre-crack position

16%. This decrease in values also occurred due to the interruption of the tensile field of stress transfer in the shear wall. The decrease in strength can be clearly seen due to the breaking of the tensile bands around the cracks and the buckling phenomenon with the increase in displacement amplitude. Also, the increasing behavior of lateral load after yielding in the drawn diagrams is caused by the strain hardening behavior of steel materials. Table 1 shows the indices of yield strength, final consistency, stiffness and ductility of the samples. Ductility is one of the important indicators to evaluate the lateral performance of the structure. Displacement ductility factor can be calculated as the ratio of failure displacement to yield displacement. The results show that all samples have good ductility in the mode of cracks under 120 mm.

#### 6-2. Effect of Crack Length in Shear Wall

In this part, the impact of the crack length in the shear wall on the lateral behavior of the shear wall has been investigated. In Figure 5, 15 curves are drawn, in each curve 4 graphs are drawn for 3 different modes of pre-crack length. In each group of steel shear walls, the position of the crack, the type of the fixed steel panel, and the length of the crack have been investigated in modes without cracks and with cracks of 30, 120, and 240 mm in length. Crack lengths of 120 and 240 mm have a significant effect on the distribution and transfer of stress in the tensile field, and the values of stiffness, ultimate strength and ductility indices and their percentage changes are given in Table 3. By changing the length of the crack in the modes of the steel shear wall that has the position of the crack C and D, there is a significant reduction in the structural indices of the wall. The reduction of stiffness indices for the shear wall with different crack positions and with LYP material has been achieved in the range of 20-50%, the ultimate strength index has decreased in the range of 4-16% and the ductility has been achieved with a decreasing trend of 28-51%. This decrease in values also occurred due to the interruption of the tensile field of stress transfer in the shear wall. The reduction of stiffness indices for the shear wall with different crack positions and with St37 material is in the range of 10 to 32%, the ultimate strength index is reduced in the range of 5 to 24%, and the ductility is also achieved with a decreasing trend of 28 to 60%. The reduction of stiffness indices for the shear wall with

different crack positions and with St52 material has been achieved in the range of 8 to 35%, the ultimate strength index has decreased in the range of 2 to 24%, and the ductility has been achieved with a decreasing trend of 26 to 58%. The stiffness of the edge column has a great impact on the lateral bearing capacity of the shear wall structures, which are designed with high stiffness. Since the aim of steel panel research is pre-crack investigation, the results showed that the tensile fields are transferred to the edge beam and the effect of the tensile fields on the edge beam is compensated by the upper and lower adjacent panels. If the pre-cracks have a length of 240 mm, buckling failure occurs due to the interruption of the tensile field, the load-carrying capacity is greatly reduced and the energy dissipation capacity is lost, and this capacity intensification is more evident in the cracks in position C and D.

#### 6-3. Impact of Shear Wall Steel Material

In this part, the impact of the steel material in the shear wall on the lateral behavior of the shear wall has been investigated. In Figure 6, 15 curves are drawn, in each curve 4 graphs are drawn for 3 different types of shear wall steel. In each group of steel shear walls, the crack position and fixed crack length and the steel material of the shear wall in LYP, St37 and St52 modes have been studied. The yield stress and final stress of different steels had a significant impact on the stress distribution in the tensile field and the values of the stiffness, ultimate strength and ductility indices and their percentage changes, which are given in Table 4. The increase in stiffness indices for the shear wall with St37 and St52 steel in the range of 2.53 to 3.63 times the stiffness of the LYP shear wall, the increased final strength index is equivalent to 1.1 to 1.45 times the strength of the LYP shear wall and the ductility has also been achieved with a decreasing trend of 8-30% compared to the shear wall with LYP material. This decrease in ductility values is achieved due to the high stiffness and strength of St37 and St52 steel materials compared to LYP steel.

#### 6-4. Study on the Damage modes of Shear Wall with Pre-crack and Opening

In this part, the damage modes of the shear wall with pre-crack and opening for two types of cracks have been studied. Cumulative plastic strain (PEEQ) has been used to examine damage modes. This output shows the locations prone to crack growth and



Table 2 - Values of indices of steel shear wall with pre-crack

Shear wall name	Yield force (kN)	Stiffness (kN/mm)	Strength (kN)	Ductility	Shear wall name	Yield force (kN)	Stiffness (kN/mm)	Strength (kN)	Ductility	Shear wall name	Yield force (kN)	Stiffness (kN/mm)	Strength (kN)	Ductility
DSW-N-0-LYP	347.04	31.37	1058.99	9.04	DSW-N-0-St37	488.2	79.42	1286.39	8.3	DSW-N-0-St52	499.81	81.31	1523.85	7.81
DSW-A-30-LYP	427.98	25.49	1057.97	6.55	DSW-A-30-St37	600.82	71.56	1284.85	6.14	DSW-A-30-St52	617.06	73.5	1521.64	5.72
DSW-A-120-LYP	437.77	23.03	1035.52	5.79	DSW-A-120-St37	635.65	66.87	1256.46	5.47	DSW-A-120-St52	697.72	73.4	1487.82	5.05
DSW-A-240-LYP	351.83	21.88	975.89	5.47	DSW-A-240-St37	492.84	61.3	1119.58	4.48	DSW-A-240-St52	539.98	67.16	1320.94	4.18
DSW-H-30-LYP	463.97	23.48	1059.94	5.57	DSW-H-30-St37	664.08	67.21	1285.81	5.32	DSW-H-30-St52	732.68	74.15	1523.36	4.86
DSW-H-120-LYP	451.61	21.55	1011.37	5.25	DSW-H-120-St37	653.54	62.36	1226.57	4.96	DSW-H-120-St52	742.55	70.85	1467.45	4.58
DSW-H-240-LYP	321.58	19.36	964.49	4.97	DSW-H-240-St37	523.99	63.08	1101.32	4.28	DSW-H-240-St52	563.67	64.47	1314.94	3.99
DSW-R-30-LYP	463.14	23.28	1058.66	5.53	DSW-R-30-St37	666.48	67.01	1286.31	5.18	DSW-R-30-St52	742.03	74.6	1523.96	4.83
DSW-R-120-LYP	435.35	20.63	1001.62	5.21	DSW-R-120-St37	638.17	60.49	1190.75	4.93	DSW-R-120-St52	721.95	68.43	1424.32	4.55
DSW-R-240-LYP	267.19	17.95	954.49	5.02	DSW-R-240-St37	459.78	61.77	1074.33	4.71	DSW-R-240-St52	496.24	63.34	1298.75	4.39
DSW-C-120-LYP	456.07	23.74	1058.74	5.73	DSW-C-30-St37	649.16	67.58	1286.13	5.47	DSW-C-30-St52	718.64	74.81	1523.39	5
DSW-C-240-LYP	439.52	18.67	985.21	4.67	DSW-C-120-St37	649.87	55.21	1132.3	4.33	DSW-C-120-St52	748.56	63.59	1378.65	4.08
DSW-C-30-LYP	285.68	15.66	926.2	4.4	DSW-C-240-St37	517.99	56.8	1066.23	3.73	DSW-C-240-St52	573.72	55.99	1232.8	3.47
DSW-D-30-LYP	470.27	21.71	1057.7	5.08	DSW-D-30-St37	699.82	64.61	1285.77	4.8	DSW-D-30-St52	780.84	72.1	1522.99	4.43
DSW-D-120-LYP	424.26	18.82	950.46	4.88	DSW-D-120-St37	626.9	55.63	1123.66	4.57	DSW-D-120-St52	719.42	63.84	1339.87	4.26
DSW-D-240-LYP	331.42	16.89	894.75	4.48	DSW-D-240-St37	532.65	54.28	980.33	3.43	DSW-D-240-St52	613.38	53.13	1159.81	3.13

Table 3- The ratio of changes in steel shear wall indices with the change of pre-crack length

Shear wall name	Stiffness ratio	Strength ratio	Ductility ratio	Shear wall name	Stiffness ratio	Strength ratio	Ductility ratio
DSW-N-0-LYP	1	1	1	DSW-R-120-St37	0.76	0.93	0.58
DSW-A-30-LYP	0.81	1	0.72	DSW-R-240-St37	0.78	0.84	0.57
DSW-A-120-LYP	0.73	0.98	0.64	DSW-C-30-St37	0.85	1	0.68
DSW-A-240-LYP	0.7	0.92	0.61	DSW-C-120-St37	0.7	0.98	0.62
DSW-H-30-LYP	0.75	1	0.62	DSW-C-240-St37	0.72	0.83	0.45
DSW-H-120-LYP	0.69	0.96	0.58	DSW-D-30-St37	0.81	1	0.58
DSW-H-240-LYP	0.62	0.91	0.55	DSW-D-120-St37	0.7	0.87	0.55
DSW-R-30-LYP	0.74	1	0.61	DSW-D-240-St37	0.69	0.76	0.41
DSW-R-120-LYP	0.66	0.95	0.58	DSW-A-0-St52	1	1	1
DSW-R-240-LYP	0.57	0.9	0.56	DSW-A-30-St52	0.9	1	0.73
DSW-C-30-LYP	0.76	1	0.63	DSW-A-120-St52	0.9	0.98	0.65
DSW-C-120-LYP	0.6	0.93	0.62	DSW-A-240-St52	0.82	0.97	0.64
DSW-C-240-LYP	0.5	0.81	0.49	DSW-H-30-St52	0.91	1	0.62
DSW-D-30-LYP	0.69	1	0.56	DSW-H-120-St52	0.87	0.96	0.59
DSW-D-120-LYP	0.6	0.9	0.54	DSW-H-240-St52	0.79	0.86	0.51
DSW-D-240-LYP	0.64	0.84	0.5	DSW-R-30-St52	0.92	1	0.62
DSW-N-0-St37	1	1	1	DSW-R-120-St52	0.84	0.93	0.58
DSW-A-30-St37	0.9	1	0.74	DSW-R-240-St52	0.78	0.85	0.56
DSW-A-120-St37	0.84	0.98	0.66	DSW-C-30-St52	0.92	1	0.64
DSW-A-240-St37	0.77	0.91	0.64	DSW-C-120-St52	0.76	0.9	0.62
DSW-H-30-St37	0.85	1	0.64	DSW-C-240-St52	0.69	0.81	0.44
DSW-H-120-St37	0.79	0.95	0.6	DSW-D-30-St52	0.89	1	0.57
DSW-H-240-St37	0.79	0.96	0.52	DSW-D-120-St52	0.79	0.86	0.55
DSW-R-30-St37	0.84	1	0.62	DSW-D-240-St52	0.65	0.78	0.4

Table 4- The ratio of changes in the indices of steel shear wall with the change of steel type of steel sheet

Shear wall name	Stiffness ratio	Strength ratio	Ductility ratio	Shear wall name	Stiffness ratio	Strength ratio	Ductility ratio
DSW-N-0-LYP	1	1	1	DSW-R-120-LYP	1	1	1
DSW-N-0-St37	2.53	1.21	0.92	DSW-R-120-St37	2.93	1.18	0.95
DSW-N-0-St52	2.59	1.44	0.86	DSW-R-120-St52	3.32	1.42	0.87
DSW-A-30-LYP	1	1	1	DSW-R-240-LYP	1	1	1
DSW-A-30-St37	2.81	1.21	0.94	DSW-R-240-St37	3.44	1.11	0.94
DSW-A-30-St52	2.88	1.44	0.87	DSW-R-240-St52	3.93	1.36	0.87
DSW-A-120-LYP	1	1	1	DSW-C-30-LYP	1	1	1
DSW-A-120-St37	2.9	1.21	0.95	DSW-C-30-St37	2.95	1.21	0.96
DSW-A-120-St52	3.19	1.44	0.87	DSW-C-30-St52	3.15	1.44	0.87
DSW-A-240-LYP	1	1	1	DSW-C-120-LYP	1	1	1
DSW-A-240-St37	2.8	1.15	0.82	DSW-C-120-St37	2.96	1.15	0.93
DSW-A-240-St52	3.07	1.35	0.76	DSW-C-120-St52	3.41	1.4	0.87
DSW-H-30-LYP	1	1	1	DSW-C-240-LYP	1	1	1
DSW-H-30-St37	2.86	1.21	0.96	DSW-C-240-St37	3.63	1.15	0.85
DSW-H-30-St52	3.16	1.44	0.87	DSW-C-240-St52	3.97	1.33	0.79
DSW-H-120-LYP	1	1	1	DSW-D-30-LYP	1	1	1
DSW-H-120-St37	2.89	1.21	0.95	DSW-D-30-St37	2.98	1.22	0.95
DSW-H-120-St52	3.29	1.45	0.87	DSW-D-30-St52	3.32	1.44	0.87
DSW-H-240-LYP	1	1	1	DSW-D-120-LYP	1	1	1
DSW-H-240-St37	3.26	1.14	0.86	DSW-D-120-St37	2.96	1.18	0.94
DSW-H-240-St52	3.33	1.36	0.8	DSW-D-120-St52	3.39	1.41	0.87
DSW-R-30-LYP	1	1	1	DSW-D-240-LYP	1	1	1
DSW-R-30-St37	2.88	1.22	0.94	DSW-D-240-St37	3.21	1.1	0.78
DSW-R-30-St52	3.2	1.44	0.87	DSW-D-240-St52	3.15	1.3	0.7

damage in the shear wall as shown in Figures 7 and 8. The concentration distribution of plastic strain damage in the pre-cracks of the upright mode in the middle of the shear wall at the relative displacement angle of the filler sheet 0.5% has reached the plastic value and at the relative displacement angle of the boundary members the yield stress (von Mises) at 0.9%. First, the circulation occurred locally in the horizontal corrugated filler sheet with a circular

opening and a pre-crack in the middle of the steel sheet and the corner of the pre-crack, and with the increase of the period of stress concentration and plastic strain in the upper and lower corners of these openings, and led to the growth of the circulation in the area around the opening and pre-cracks and local buckling have been created and yield stresses have developed in the beam and column members. And the progress of this circulation, has increased and turned



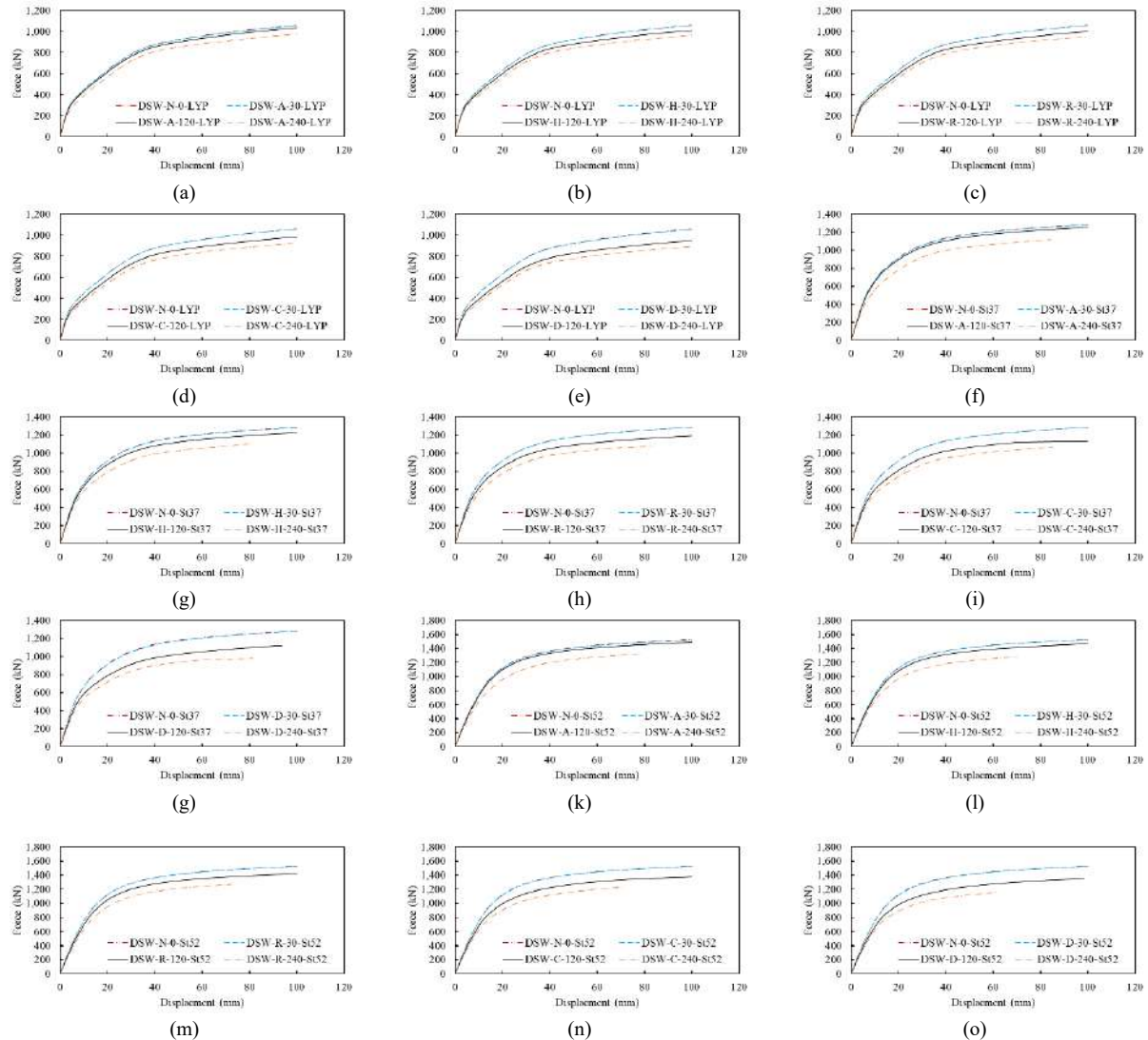


Figure 5 – Comparison of force-displacement curves for pre-crack length

into general buckling on the surface of the filler sheet, especially around the pre-cracks. An example of cumulative plastic strain and damage mode of the steel frame at 3% circulation is shown in Figures 7 and 8. The results of this study showed that the geometric stiffness and high resistance to general buckling and the concentration of buckling around the openings and pre-cracks depend on the position of the pre-crack and the tensile field of the wall. In general, cracks D and C with sizes of 120 and 240

mm have shown the most critical condition and the highest strain with values above 0.15, which means that the elements in this area are prone to the initiation of sheet tearing and crack growth.

## 7. Conclusion

In this article, 48 samples of steel sheet shear wall with circular opening and pre-crack with three-story frame and one opening were examined under axial and pushover loads to investigate the lateral behavior.

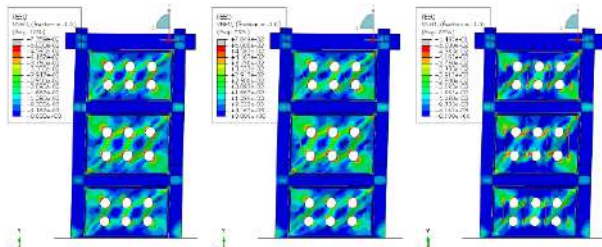


Figure 7 - Distribution of plastic strain damage concentration in the pre-cracks of the upright mode in the middle of the shear wall

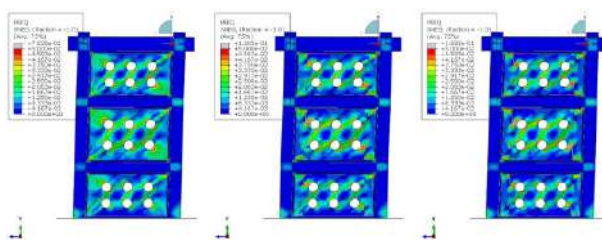


Figure 8 - Distribution of plastic strain damage concentration in the pre-cracks of the upright mode at the corner of the shear wall

The models made by the nonlinear finite element method of the steel sheet shear wall structure were confirmed with the test results.

Further, by examining the stiffness, resistance and ductility indicators of the wall, the following results were obtained:

Different steel sheet shear walls structures with opening and pre-crack for crack lengths of 120 to 240 mm showed low strength, stiffness and ductility, and the ductility coefficients were less than 5. The crack length and crack position parameters have a great impact on the ductility capacity, while they have little impact on the initial stiffness and strength. Horizontal cracks located at the top or bottom at the corners of the frame (positions C and D) had a great impact on the lateral behavior and reduced ductility by 60% and wall strength by 32%. Because these cracks cut the stress transmission path in the tensile field and the capacity of the wall is greatly reduced, in the mode of pre-crack with a length of 30 mm, the final strength of the wall did not change, but the stiffness and ductility decreased by 10 and 15%, respectively. By increasing the crack length from 30 to 120 mm, the ultimate strength, stiffness and ductility of the wall decreased by 6, 26 and 33%, respectively, and by changing the crack length from 30 to 240 mm, the ultimate strength, stiffness and ductility decreased by 11, 39 and 46%, respectively. Also, by changing the

shear wall steel sheet material from LYP steel to St37 and St52, the ultimate strength and stiffness have increased by 3.63 and 1.45 times, respectively, and the ductility has decreased by 30%.

## 8. References

- [1]. Thorburn, L. J., Montgomery, C. J., & Kulak, G. L. (1983). Analysis of steel plate shear walls.
- [2]. Elgaaly, M., & Liu, Y. (1997). Analysis of thin-steel-plate shear walls. *Journal of Structural Engineering*, 123(11), 1487-1496.
- [3]. Caccese, V., Elgaaly, M., & Chen, R. (1993). Experimental study of thin steel-plate shear walls under cyclic load. *Journal of Structural Engineering*, 119(2), 573-587.
- [4]. Alavi, E., & Nateghi, F. (2009). Non-linear behavior and shear strength of diagonally stiffened steel plate shear walls. *International Journal of Engineering*, 22(4), 343-356.
- [5]. Alinia, M. M., & Shirazi, R. S. (2009). On the design of stiffeners in steel plate shear walls. *Journal of Constructional Steel Research*, 65(10-11), 2069-2077.
- [6]. Driver, R. G., Kulak, G. L., Kennedy, D. L., & Elwi, A. E. (1998). Cyclic test of four-story steel plate shear wall. *Journal of Structural Engineering*, 124(2), 112-120.
- [7]. Guo, H. C., Hao, J. P., & Liu, Y. H. (2015). Behavior of stiffened and unstiffened steel plate shear walls considering joint properties. *Thin-Walled Structures*, 97, 53-62.
- [8]. Sigariyazd, M. A., Joghataie, A., & Attari, N. K. (2016). Analysis and design recommendations for diagonally stiffened steel plate shear walls. *Thin-Walled Structures*, 103, 72-80.
- [9]. Alavi, E., & Nateghi, F. (2013). Experimental study on diagonally stiffened steel plate shear walls with central perforation. *Journal of Constructional Steel Research*, 89, 9-20.
- [10]. Alavi, E., & Nateghi, F. (2013). Experimental study of diagonally stiffened steel plate shear walls. *Journal of Structural Engineering*, 139(11), 1795-1811.
- [11]. Du, Y., Hao, J., Yu, J., Yu, H., Deng, B., Lv, D., & Liang, Z. (2018). Seismic performance of a repaired thin steel plate shear wall structure. *Journal of Constructional Steel Research*, 151, 194-203.

- [12]. Xu, L., Liu, J., & Li, Z. (2021). Parametric analysis and failure mode of steel plate shear wall with self-centering braces. *Engineering Structures*, 237, 112151.
- [13]. Tong, J. Z., & Guo, Y. L. (2015). Elastic buckling behavior of steel trapezoidal corrugated shear walls with vertical stiffeners. *Thin-Walled Structures*, 95, 31-39.
- [14]. Xu, Z., Tong, G., & Zhang, L. (2018). Elastic and elastic-plastic threshold stiffness of stiffened steel plate walls in compression. *Journal of Constructional Steel Research*, 148, 138-153.
- [15]. Gen-shu, T. O. N. G., & Wen-deng, T. A. O. (2013). Elastic shear buckling of steel shear walls strengthened vertically by closed section stiffeners. 30(9), 1-9.
- [16]. Nie, J. G., Zhu, L., Fan, J. S., & Mo, Y. L. (2013). Lateral resistance capacity of stiffened steel plate shear walls. *Thin-Walled Structures*, 67, 155-167.
- [17]. Hosseinzadeh, S. A. A., & Tehranizadeh, M. (2012). Introduction of stiffened large rectangular openings in steel plate shear walls. *Journal of Constructional Steel Research*, 77, 180-192.
- [18]. Sabouri-Ghomi, S., & Mamazizi, S. (2015). Experimental investigation on stiffened steel plate shear walls with two rectangular openings. *Thin-Walled Structures*, 86, 56-66.
- [19]. Shekastehband, B., Azaraxsh, A., & Showkati, H. (2017). Experimental and numerical study on seismic behavior of LYS and HYS steel plate shear walls connected to frame beams only. *Archives of civil and mechanical engineering*, 17(1), 154-168.
- [20]. Berman, J. W., & Bruneau, M. (2005). Experimental investigation of light-gauge steel plate shear walls. *Journal of Structural Engineering*, 131(2), 259-267.
- [21]. Vian, D., Bruneau, M., & Purba, R. (2009). Special perforated steel plate shear walls with reduced beam section anchor beams. II: Analysis and design recommendations. *Journal of Structural Engineering*, 135(3), 221-228.
- [22]. Purba, R., & Bruneau, M. (2009). Finite-element investigation and design recommendations for perforated steel plate shear walls. *Journal of structural engineering*, 135(11), 1367-1376.
- [23]. Purba, R., & Bruneau, M. (2009). Finite-element investigation and design recommendations for perforated steel plate shear walls. *Journal of structural engineering*, 135(11), 1367-1376.
- [24]. Guo, L., Rong, Q., Ma, X., & Zhang, S. (2011). Behavior of steel plate shear wall connected to frame beams only. *International Journal of Steel Structures*, 11(4), 467-479.
- [25]. Vatansever, C., & Yardimci, N. (2011). Experimental investigation of thin steel plate shear walls with different infill-to-boundary frame connections. *Steel and Composite Structures*, 11(3), 251-271.
- [26]. Shekastehband, B., Azaraxsh, A. A., Showkati, H., & Pavir, A. (2017). Behavior of semi-supported steel shear walls: Experimental and numerical simulations. *Engineering structures*, 135, 161-176.
- [27]. Wei, M. W., Liew, J. R., Yong, D., & Fu, X. Y. (2017). Experimental and numerical investigation of novel partially connected steel plate shear walls. *Journal of Constructional Steel Research*, 132, 1-15.
- [28]. Documentation, A., & Manual, U. (2010). Version 6.14. Dassault systemes.
- [29]. Wang, M., Shi, Y., Xu, J., Yang, W., & Li, Y. (2015). Experimental and numerical study of unstiffened steel plate shear wall structures. *Journal of Constructional Steel Research*, 112, 373-386.



## Pervious concrete as environmentally friendly materials-an overview

Shahriar Gholamin <sup>a,\*</sup>

<sup>a</sup>First affiliation, Address, City and Postcode, Country

Department of Civil Engineering , Bandar Anzali Branch, Islamic Azad University, Bandar Anzali , Iran

**Journals-Researchers use only:** Received date 2022 September 3; revised date 2022 October 10; accepted date 2022 October 16

---

### Abstract

Pervious concrete contains a mixture of water, cement, coarse aggregates and little or no fine aggregates. Pervious concrete is increasingly known as an environmentally friendly material due to its usefulness in improving water quality by removing all suspended solid particles in the flood, reducing the flow of flood water, reducing the heat island effect and other environmental benefits. In this article, the results of valid research on the physical (slump, density, porosity, water permeability) and mechanical (compressive strength, flexural strength, splitting tensile strength) properties of Pervious concrete have been briefed and reported. © 2017 Journals-Researchers. All rights reserved. (DOI:<https://doi.org/10.52547/JCER.4.2.34>)

**Keywords:** Pervious concrete, porosity, permeability, environmentally friendly, mechanical properties

---

### 1. Introduction

Concrete pavement is known as a pavement with a long life. The use of conventional concrete as a

paving material has caused some problems such as drainage for the flow of water caused by floods, as well as high noise compared to other types of pavements. Considering the negative effects of conventional concrete paving, the idea of using Pervious concrete (also called porous concrete or

\* Corresponding author. Tel.: +989113856939 ; e-mail: [sh.gholamin@gmail.com](mailto:sh.gholamin@gmail.com)

concrete with improved pores) in paving streets and sidewalks has been proposed for about 150 years [1,2]. Pervious concrete includes a mixture of water, cement, coarse aggregates and little or no fine aggregates [3,4]. Because Pervious concrete has a lot of empty space, its density, compressive strength and thermal conductivity are lower than normal concrete [5]. Pervious concrete is increasingly used due to its usefulness in improving water quality by removing all suspended solid particles in the flood, reducing the flow of flood water (Fig.1) and improving the sliding resistance of the pavement by rapid water drainage during storm events, reducing Sound leveling on the site, improving the visibility of the pavement surface,

reducing the heat island effect, are used [1,6,7]. Therefore, Pervious concrete can be used as an environmentally friendly material in pavements with low traffic volumes, roads, alleys, urban streets, crossings and sidewalks, open parking areas, tennis courts, and as a base for conventional concrete pavements. , patio (private yard), artificial rocks, slope consolidation, tree network on sidewalks, hydraulic structures, drainage edge of pavements, sound insulation, load-bearing walls [6]. In this article, the results of valid research on the physical and mechanical properties of Pervious concrete have been briefed and reported.

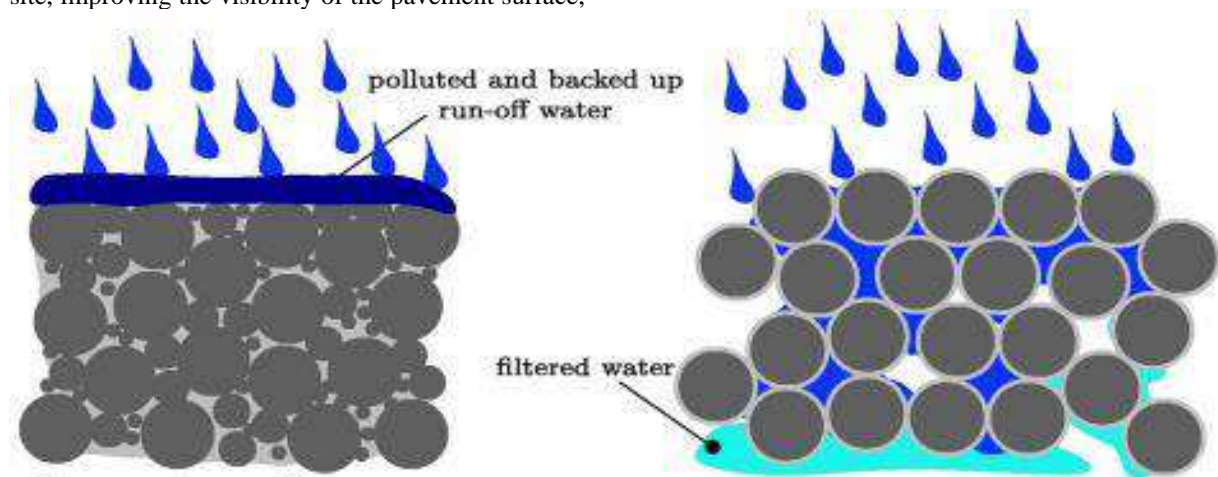


Fig . 1. Comparison of impervious concrete and pervious concrete [8].

## 2. Physical properties

### 2.1. Slump

Fresh Pervious concrete is very hard due to its water-to-cement ratio and low volume of cement paste, so it has low or even zero slump [9]. In the research of El-Hassan et al. [10], for the ratio of  $W / C = 0.4$ , the slump is in the range of 35-81 mm, while in the research of Nguyen et al. [9], for the ratio of  $W / C = 0.3$ , the slump is zero (Fig. 2 ) has been reported.



Fig. 2. Consistency of fresh Pervious concrete [9].



## 2.2. Density

Sata et al. [5], in a research, used natural limestone (NA), recycled concrete (RC) and recycled clay brick (RB) in the form of coarse aggregate in the size of 4.5-9.75 mm to make Pervious geopolymer concrete (PGC) (Fig. 3). The density of Pervious concrete with NA, RC and RB were reported in the range of 1710-1730 and 1420-1520 kg/m<sup>3</sup>, respectively. Cosic et al. [3], in a research of dolomite aggregate in sizes 0-4, 4-8, 8-16 mm, 10% sand in size 0-2 mm and steel slag in sizes 16-8, 8-4 mm, used 10% sand in the size of 0-2 mm to make Pervious concrete. The results of their research showed the density of Pervious concrete in the range of 2076.6 - 2442.4 kg/m<sup>3</sup>.



(a) NA



(b) RC



(c) RB

Fig. 3. Comparison of coarse aggregate [5].

## 2.3. porosity

Total porosity is the sum of open and closed porosity in Pervious concrete and depends on aggregate porosity and binder amount. Open porosity (Fig. 4) is the effective porosity for water flow to pass through hardened Pervious concrete. In the research of Tennis et al. [6], the of open porosity for the passage of water flow through Pervious concrete was reported as 15-25%. In the researches of Huang et al. [1], Chindaprasir et al. [2], Cosic et al. [3], Zhang et al. [4], Sata et al. [5], the of total porosity is 20%-30%, 15%-25%, respectively. , 6.3%-22.2%, 15.1%-16.5%, 21.7%-27.4% have been found. The recommended value for the of total porosity according to ACI 522 [11] is 18%-35%.

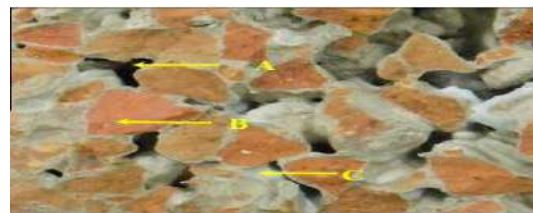


Fig. 4. Fracture surface of PGC containing RB ; (A) open porosity ; (B) fractured RB ; (C) geopolymer paste [5]

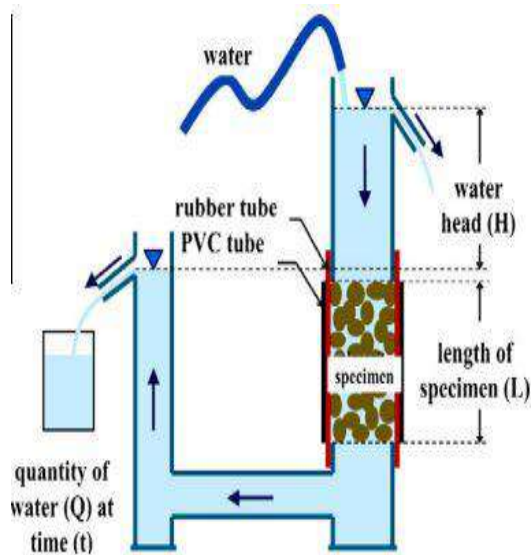


Fig. 5a. The device for measuring water permeability coefficient by constant head method [5].

Fig. 5. The device for measuring water permeability coefficient

In the researches of Tennis et al. [6], Huang et al. [1], Zhang et al. [4], Sata et al. [5] and Lee et al. [12], the water permeability coefficient is 2-5.4 mm/s, 10-20 mm/s, 3.1-3.8 mm/s, 7.1-17.1 mm/s and 1.2-18.4 mm/s have been reported respectively. The recommended value for the water permeability coefficient according to ACI 522 [11] should be more than 1mm/s. The results of Huang et al.'s research [1] showed that three types of single size coarse aggregates (4.75, 9.5, 12.5mm) did not have a great impact on porosity and permeability coefficient. Also adding latex and sand reduced a small amount of porosity and permeability coefficient, but the simultaneous combination of latex, sand and fibers did not reduce porosity and permeability coefficient.

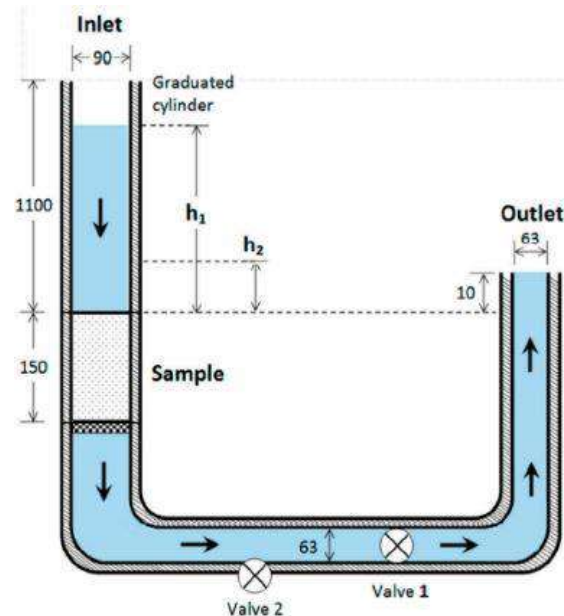


Fig. 5b. The device for measuring water permeability coefficient by falling head method [12].

### 3. Mecanical properties

#### 3.1. Compressive strength

In their research, Sata et al [5] investigated the 7-day compressive strength of cylindrical samples with a diameter of 100 mm and a height of 200 mm. The compressive strength for NA, RC and RB mixtures was reported in the range of 11.9-13.6 Mpa, 7-11.3 Mpa and 2.9-6.6 Mpa, respectively. In their research, they found that like conventional concrete with increasing density, the compressive strength as shown in Figure 6 Given, it improves. In their research, Cosic et al. [3] investigated the 28-day compressive strength of 150 mm cubic samples. They reported compressive strength in the range of 20.2-69.5 Mpa. In the study of Chindaprasir et al [2], the compressive strength of cylindrical samples with a diameter of 100 mm and a height of 200 mm for total porosities of 15%, 20% and 25% were found in the range of 38-44 Mpa, 29-35 Mpa and 15-22 Mpa, respectively. Huang et al. [1] reported the 7-day

compressive strength of cylindrical specimens with a diameter of 152 mm and a height of 305 mm in the range of 15-5 Mpa. In their research, they found that replacing natural coarse aggregate with 7% sand and replacing 10% cement with latex improves the compressive strength compared to the control sample. Adding fibers in samples without sand and latex also improves the compressive strength. Mixtures with sand, fibers and latex did not improve the compressive strength further. Zhang et al. [4] reported the 28-day compressive strength of rectangular cube samples with dimensions of 150\*150\*300 mm in the range of 15.5-24.2 Mpa. In their research, they found that with the increase of the crushing index, the compressive strength decreased. Lee et al. [12] reported the 28-day compressive strength of cylindrical samples with a diameter of 100 mm and a height of 200 mm in the range of 12.6-52.76 Mpa. They found that the 90-day and 28-day compressive strength values are close to each other, and the addition of glass and steel fibers increases the compressive strength.

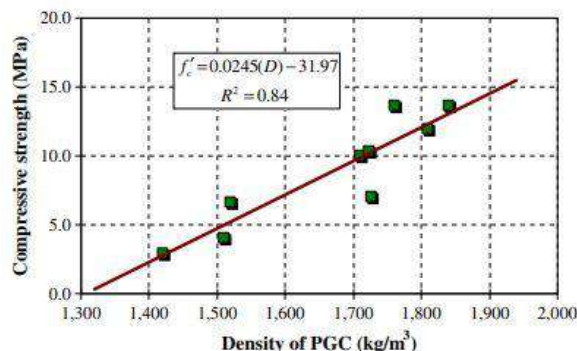


Fig. 6. Relationship between compressive strength at the age of 7 days and density of PGC [5].

### 3.2. flexural strength

In their research, Cosic et al [3] investigated the 28-day flexural strength of rectangular cube samples with dimensions of 100\*100\*400 mm. They reported flexural strength in the range of 4-9.7 Mpa. Zhang et al. [4] reported the 28-day flexural strength of rectangular cube samples with dimensions of

150\*150\*600 mm in the range of 2.55-3.56 Mpa. In their research, they found that with the increase of the crushing index, the flexural strength decreased. Lee et al. [12] reported the 28-day flexural strength of 100\*100\*350mm rectangular cube samples in the range of 3.02-8.48 Mpa. They found that the addition of glass and steel fibers resulted in increased flexural strength. El-Hassan et al [10] in their research used rectangular cube samples with dimensions of 150\*150\*450 mm to test the flexural strength. The results of their research showed the flexural strength at the age of 28 days in the range of 0.93-3.15 Mpa.

### 3.3. Splitting tensile strength

In their research, Sata et al. [5] investigated the 7-day splitting tensile strength of cylindrical specimens with a diameter of 100 mm and a height of 200 mm. Splitting tensile strength for NA, RC and RB mixtures was reported in the range of 1.5-1.8 Mpa, 1.3-1.5 Mpa and 0.4-0.9 Mpa, respectively. Huang et al. [1] reported the 7-day splitting tensile strength of cylindrical specimens with a diameter of 152 mm and a height of 76 mm in the range of 0.55-1.9 Mpa. They found that mixing with aggregates with a smaller diameter resulted in Pervious concrete with higher splitting tensile strength, and the effect of replacing coarse aggregate with sand sometimes caused a decrease in tensile split strength. Replacing cement with latex and adding fibers increased the splitting tensile strength. Nguyen et al. [9] reported the splitting tensile strength for cubic specimens with dimensions of 150 \* 150 \*150 mm at the age of 28 days in the range of 1.78-2.56 Mpa (Figure 7a). They found that the splitting tensile strength ( $R_t$ ) is proportional to the compressive strength ( $R_c$ ) and their relationship is linear (Figure 7b). El-Hassan et al. [10] in their research used cylindrical samples with a diameter of 150 mm and a height of 300 mm to test the splitting tensile strength. The results of their research showed the splitting tensile strength at the age of 28 days in the range of 0.68-3.1 Mpa.



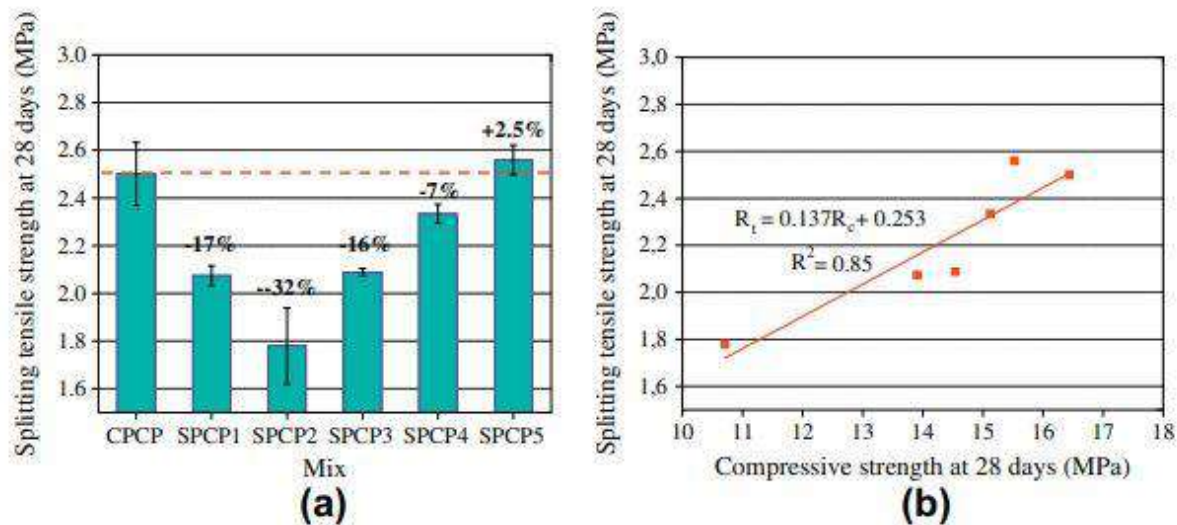


Fig. 7. splitting tensile strength test at 28 days (a) and relation between splitting tensile strength and compressive strength (b) [9].

#### 4. Conclusion

In this article, the physical and mechanical properties of Pervious concrete in the researches conducted in the past are reported in summary form. The most important results of these studies are as follows:

1) Slump of Pervious concrete is less than conventional concrete and can even be zero. Slump of Pervious concrete is dependent on the ratio of water to cement and the amount of cement paste. The maximum slump of Pervious concrete has been reported 81mm with a ratio of  $W/C = 0.4$ .

2) The density of Pervious concrete is lower than the density of conventional concrete due to higher porosity, which depends on the density of aggregate and the amount of cement paste. The density value of Pervious concrete is reported in the range of 1420-2442.4 kg/m<sup>3</sup>.

3) Total and open porosity have been reported in the range of 6.3%-30% and 15%-25%, respectively, and the recommended value for total porosity according to ACI 522 [11] is 18%-35%.

4) The water permeability coefficient was reported in the range of 1.2-18.4 mm/s, which was higher than the minimum recommended value according to ACI 522 [11].

5) Pervious concretes had lower compressive strength due to higher porosity than conventional concretes. The compressive strength depended on the type and amount of binder and aggregate strength. The 28-day compressive strength of cylindrical samples with a diameter of 100 mm and a height of 200 mm has been reported in the range of 12.6-52.76 Mpa. Like conventional concrete, the compressive strength increased linearly with the increase of density in Pervious concrete.

6) The 28-day flexural strength of Pervious concrete is reported in the range of 0.93-9.7 Mpa, and the addition of glass and steel fibers increased the flexural strength.

7) 28-day splitting tensile strength of Pervious concrete, considering the type of sample, has been reported in the range of 0.68-3.1 Mpa, and replacing cement with latex and adding fibers in the mixture increased the splitting tensile strength.

#### References

- [1] Huang, B., Wu, H., Shu, X., Burdette, E.G.(2010). Laboratory evaluation of permeability and strength of polymer-modified pervious concrete . Construction and Building Materials,24(5) , 818-823.
- [2] Chindaprasirt, P., Hatanaka, S., Chareerat T., Mishima, N., Yuasa, Y.(2008). Cement paste characteristics and porous

- concrete properties. *Construction and Building Materials*, 22 (5), 894–901.
- [3] Cosic, K., Korat, L., Ducman, V., Netinger, I.(2015). Influence of aggregate type and size on properties of pervious concrete. *Construction and Building Materials*, 78 , 206–213.
- [4] Zhang, Z., Zhang, Y., Yan, C., Liu, Y.(2017). Influence of crushing index on properties of recycled aggregates pervious concrete. *Construction and Building Materials*, 135 , 112–118.
- [5] Sata, V., Wongsu, A., Chindaprasit, P.(2013). Properties of pervious geopolymer concrete using recycled aggregates. *Construction and Building Materials*, 42, 33–9.
- [6] Tennis, P.D., Leming, M.L., Akers, D.J.(2004). Pervious Concrete Pavements, Portland Cement Association, Skokie Illinois, Silver Spring, Maryland, pp.14-36.
- [7] Takebayashi, H., Moriyama, M.(2012). Study on surface heat budget of various pavements for urban heat island mitigation. *Advances in materials science and engineering*, 2012 , 17 May, 523051.
- [8] Zhong, R., Wille, K.(2016). Compression response of normal and high strength pervious concrete. *Construction and Building Materials*, 109 , 177–187.
- [9] Nguyen, D.H., Boutouil, M., Sebaibi, N., Leleyter, L., Baraud, F.(2013). Valorization of seashell by-products in pervious concrete pavers. *Construction and Building Materials*, 49, 151–160.
- [10] El-Hassan , H., Kianmehr , P., Zouaoui , S.(2019). properties of pervious concrete incorporating recycled concrete aggregate and slag. *Construction and Building Materials*, 212 164–175.
- [11] American Concrete Institute, ACI Committee 522. (2010). Pervious concrete. Detroit
- [12] Lee, M.G., Wang, W.C., Wang, Y.C., Hsieh, Y.C., Lin, Y.C. (2022). Mechanical Properties of High Pervious Concrete with Steel Fiber or Glass Fiber. *Buildings* , 7 May, 12050620.



# The effect of steel and hybrid fibers on the impact resistance of concrete enclosed with FRP sheets

Zahed Parvinnejad <sup>a\*</sup>

<sup>a</sup> Department of Civil Engineering, Islamic Azad University of Chalous, Iran

**Journals-Researchers use only:** Received date 2022 September 5; revised date 2022 October 12; accepted date 2022 October 19

## Abstract

Due to the widespread use of concrete in all kinds of structures, the probability of its exposure to dynamic loads has increased. Since concrete is one of the most widely used materials in civil engineering, its main weakness can be pointed out, which is its brittleness and brittle performance. The use of fibers to improve the properties of concrete has been the focus of engineers for a long time. The most common fibers used to increase the impact resistance of concrete, steel and polypropylene were investigated in this research as single and hybrid fibers. In this study, by using the ACI 544-based weight projection method, the resistance of concrete against impact loading on standard cylindrical concrete samples (30 x 15) containing steel fibers and polypropylene in two cases with and without lap sheet FRPs were investigated. The results showed that the use of these fibers increases the impact resistance of concrete. Also, both CFRP and GFRP sheets that were tested improve the impact resistance of concrete and increase the number of cycles of this test. Some GFRP sheets have performed better than CFRP. Also, the presence of FRP sheets has caused a change in the type of failure compared to the absence of FRP. Also, concrete samples which fiber delay concrete breaking, significantly. © 2017 Journals-Researchers. All rights reserved. (DOI: <https://doi.org/10.52547/JCER.4.2.41>)

**Keywords:** Concrete, Impact resistance, Steel Fibers , Hybrid fibers , FRP sheets ;

## 1. Introduction

Concrete is one of the most widely used construction materials, as it is used in various construction activities such as roads, dams, tunnels, buildings, etc.

With the increase in the use of concrete, the possibility of being exposed to various loads, including static and dynamic loads, has also increased. Types of dynamic loads can include earthquakes, explosions, wind, etc. To determine the resistance of concrete against such loads, different methods have been presented [1]. One of the most common, least expensive, and at the same time the

\* Corresponding author. Tel.: +989111953894; e-mail: zahed\_parvin\_2009@yahoo.com.

simplest method is the weight throw method proposed by the ACI 544 [2] committee. This study tries to investigate the behavior of concrete samples after being subjected to impact load by the drop weight throwing method. All kinds of dynamic and static loads can cause cracks in the structures that all kinds of load-bearing elements of concrete structures are covered by FRP sheets for strengthening, it is customary that the reason is the delay in placing the damaged concrete member in the final rupture range. is. As the aim of this study, the effect of wrapping concrete samples containing steel and hybrid fibers by CFRP and GFRP sheets on the impact resistance of concrete has been investigated. For this purpose, concrete samples were made with a water-cement ratio of 0.34 and its impact resistance was investigated with and without CFRP and GFRP screws.

## 2. Mixing proportions

### 2.1. Consumable materials

In this study, type 2 Portland cement was used as an adhesive material. Its related chemical compounds are available in Table 1. River type sand and broken type sand with the largest nominal size of 12.5 mm and water absorption percentage of 0.73. Also, steel and polypropylene fibers have been used in concrete samples in a single and hybrid form. In the following, two types of CFRP and GFRP sheets are used to cover the samples under loading in order to delay the failure.

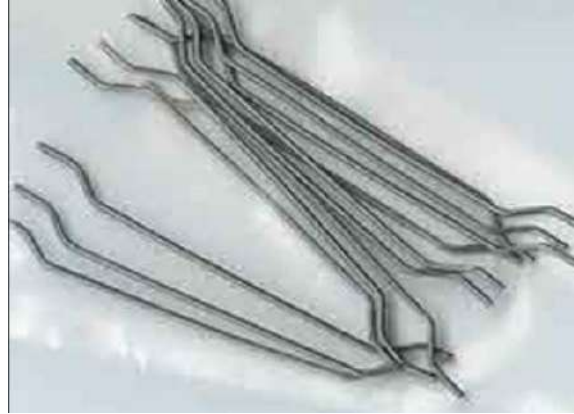


Figure 1. Steel fibers & [4].



Figure 2. Polypropylene fibers[4].

Table 1  
Characteristics of used fibers[4].

Type of fiber	Density (gr/cm <sup>3</sup> )	Tensile strength (Mpa)	Diameter (mm)	Length (mm)	Aspect ratio	Modulus of elasticity (Gpa)
Steel	7.8	1050	0.75	60	80	210
Polypropylene	$0.91 \times 10^{-3}$	350- 400	0.022	12	545	4

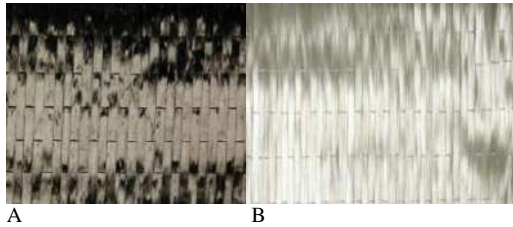


Figure 3. A CFRP &amp; B GFRP sheet.

Table 2  
Chemical properties of used cement[4].

Chemical compounds(%)	Cement
SiO <sub>2</sub>	46.21
Al <sub>2</sub> O <sub>3</sub>	55.5
Fe <sub>2</sub> O <sub>3</sub>	46.3
CaO	95.63
MgO	86.1
SO <sub>3</sub>	42.1
K <sub>2</sub> O	54.0
Na <sub>2</sub> O	26.0

## 2.2. Plans for mixing concrete and preparing samples

In this article, normal concrete samples were made with a water-cement ratio of 0.34. After making the concrete, 10 cm cubic samples were molded to perform the compressive strength test. The compressive strength was tested on the samples at the age of 28 days. Also, cylindrical standard samples of 15 x 30 cm were made to determine the impact resistance. As shown in Figure 1, to perform the impact resistance test from a hammer weighing 4.45 kg that is free-falling from a height of 7.45 cm on a steel sphere with a diameter of 6.35 cm exactly on the center of the sample. It was used as a ring (15x6.4) cm. According to the ACI 544 committee, this ball is inside a piston that prevents the ball from moving out of the center of the concrete. The significant point is that the blows must be applied to the sample

completely consecutively, and also in the concrete under test, the grading and description of the aggregates must be the same so that we can have good results. By definition, the minimum number of blows to create the first visible crack is represented by N1, and the number of blows for final failure is represented by N2.



Figure 4. A device for determining impact resistance based on ACI 544

## 3- results

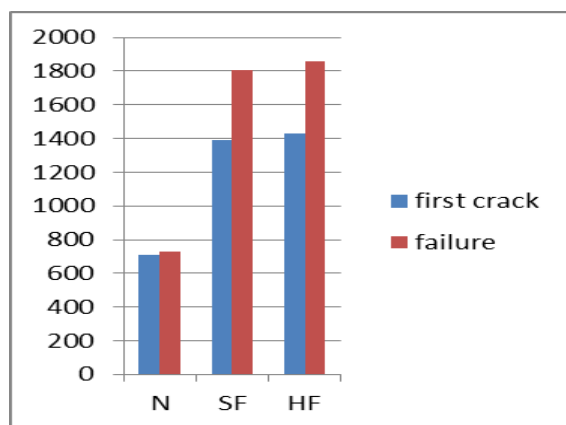
The compressive strength of ordinary concrete with steel fibers and hybrid with a water-cement ratio of 0.34 at the age of 28 days has been calculated, which is based on the average of three cubic samples of 10 cm. The concrete containing 1% steel fibers was tested, the compressive strength of this concrete was 61.7 MPa, compared to concrete with the same structure without fibers, this concrete showed an increase in strength by 10% and 6%, respectively. Also, the concrete containing the combination of steel fibers and polypropylene was investigated and its compressive strength was 59.1 MPa, the results showed that compared to the normal concrete, the strength increased by 7.2%, but compared to the concrete with 1% steel fibers, 3. It has shown an 11% decrease in resistance. These results show the high ability of steel fibers to control cracks and breakage

during load application type of concrete can be divided into high strength concrete. The impact resistance of concrete samples with and without screws and of CFRP and GFRP types was investigated, and the results are shown in Figures 2 and 3 for the first visible crack and final failure, respectively. As it can be seen, the first crack in fiber concrete without laps occurred in 1731 blows. This amount of impact in the presence of GFRP screws has been obtained in the amount of 3106 impacts. Such a situation in the presence of CFRP laps has an increase compared to concrete without laps. According to the results, it can be pointed out that the performance of FRP wrapped concrete against impact loads has improved. The final impact resistance of fiber concrete with 1832 round screw is estimated, which is about 101 impacts more than the number of impacts required for the first crack.

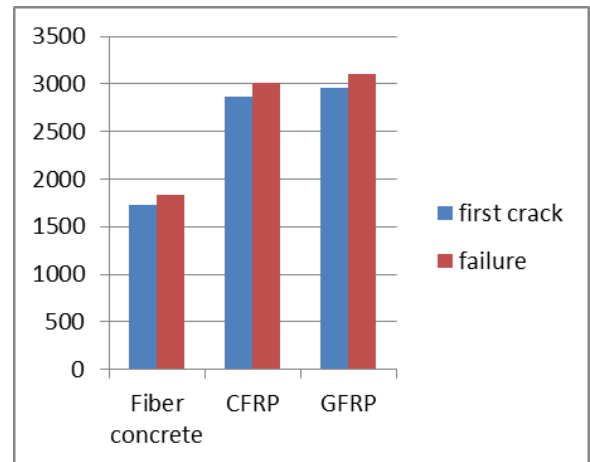
Table 3

28-day compressive strength of concrete

Type of fiber	Design type	Compressive strength (Mpa)
1	NC	54.8
2	ST (ST1)	61.7
3	HF (ST1PP0.1)	559.1

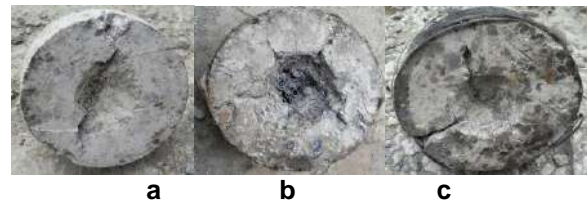


Figures 5. Impact resistance of fiber concrete



Figures 6. Impact resistance of concrete wrapped with FRP sheets

In a study by Nili and Afroughsabet [3], this number for normal concrete is 3 impacts. On the other hand, the ultimate strength of concrete wrapped with GFRP is 3106 blows, which is 152 blows more than the first visible crack.



Figures 7. Failure method in samples a. without winding , b. GFRP &amp; c. CFRP

#### 4 - Conclusion

In this study, the effect of CFRP and GFRP sheets on the resistance of concrete containing steel and hybrid fibers against impact in cases with concrete without laps has been investigated, and the following results were obtained.

1. The results showed that the use of steel and hybrid fibers were effective in increasing the impact resistance of concrete, but hybrid fibers could have a greater effect in controlling cracks and final failure in concrete.
2. The presence of GFRP screws increases the impact resistance of concrete without screws up to 1.7 times.

This situation is increased up to 1.64 times in the presence of CFRP screws.

3. The presence of both GFRP and CFRP laps improves the final rupture strength compared to concrete without laps.

4. Rounding can not only increase impact resistance, but can also increase the number of concrete blows between the first crack and the final crack, which will have an unfavorable effect on the design and performance of the structure.

5. Wrapping concrete by FRP sheets causes crack control and wide microcracks.

## References

- [1] Rahmani T, Kiani B, Shekarchi M, Safari A. Statistical and experimental analysis on the behavior of fiber reinforced concretes subjected to drop weight test. *Construction and Building Materials*;37, 360–369,2012.
- [2] ACI Committee 544.1R-96: state-of-the-art report on fiber reinforced concrete; Reapproved 2002.
- [3] Nili M, Afrouhsabet V. Combined effect of silica fume and steel fiber on the impact resistance and mechanical properties of concrete. *International Journal of Impact Engineering*;37:879-86,2010.
- [4] Nili M, Afrouhsabet V.2010 .Combined effect of silica fume and steel fiber on the impact resistance and mechanical properties of concrete. *International Journal of Impact Engineering*;37:879-86,2010
- [5] Yao W, Li J, Wu K.2003. *Cem Conc Res* 2003;33:27e30.
- [6] Bentur A, Mindness S.1990. *Fiber reinforced cementitious composites*. London and New York: Elsevier Applied Science; 1990.
- [7] Nystrom U, Gylltoft K.2011. Comparative numerical studies of projectile impacts on plain and steel-fibre reinforced concrete. *Int J Impact Eng* 2011;38:95–105.
- [8] Song PS, Wu JC, Hwang S, Sheu BC .2005. Statistical analysis of impact strength and strength reliability of steel–polypropylene hybrid fiber-reinforced concrete. *Constr Build Mater* 2005;19:1–9.





# Study of the collapse of Sardabroud-Chalous truss bridge

Morteza Jamshidi<sup>a,\*</sup>; Teymour Sam<sup>a</sup>

<sup>a</sup>Assistant Department of Civil Engineering, Islamic Azad University of Chalous, Iran

**Journals-Researchers use only:** Received date 2022 September 4; revised date 2022 October 18; accepted date 2022 October 25

## Abstract

Many of the old bridges in northern Iran, which are often more than 50 years old, are made of steel trusses. The superstructure of these bridges usually consists of two simple and parallel trusses that increase lateral stability, the upper part of these two trusses are connected using bracing elements. In some truss bridges such as the Sardabroud-Chalous bridge, the transverse brace has been removed due to the small length of the span (about 31 meters). These types of trusses that do not have transverse restraints in the upper part are called pony trusses, which have less lateral resistance due to the removal of transverse restraints. On December 25, 2009, while the trailer was passing, a steel cargo weighing about 10 tons was released from the trailer floor and thrown towards one of the vertical elements of the truss. The impact of this heavy object causes the failure of this member and the subsequent failure of the adjacent members, which eventually leads to the collapse of the entire structure. In this paper, the progressive failure mechanism of Sardabroud Bridge will be studied using ABAQUS software. The results of sensitivity analysis and Downstream analysis show that except for zero force elements, other vertical and oblique elements have significant sensitivity that should be prevented from being damaged. Interestingly, at the moment of failure and after the failure, the alternative route is the force distribution, which is mainly the forces trying to cross the pressure rim, but small deformations in a chain led to large deformations and caused the progressive failure, which destroyed the bridge in 0.7 seconds. © 2017 Journals-Researchers. All rights reserved. (DOI:<https://doi.org/10.52547/JCER.4.2.46>)

Keywords: Steel bridges, Truss, Progressive failure, Sensitivity analysis

## 1. Introduction

Many of the old bridges in northern Iran, which are often more than 50 years old, are made of steel trusses. The superstructure of these bridges usually consists of two simple and parallel trusses that to

increase lateral stability, the upper part of these two trusses are connected using bracing elements. In some truss bridges such as the Sardabroud-Chalous bridge, due to the small length of the span (about 31 meters), the transverse brace has been removed (Figure (1)). These types of trusses that do not have transverse restraints in the upper part are called pony trusses, which have less lateral resistance due to the

\* Corresponding author. Tel.: +989111912549; e-mail: m.jamshidi@iauc.ac.ir.

removal of transverse restraints. On December 25, 2009, while the trailer was passing, a steel cargo weighing about 10 tons was released from the trailer floor and thrown towards one of the vertical elements of the truss. The impact of this heavy object causes the failure of this member and the subsequent failure of the adjacent members, which eventually leads to the collapse of the entire structure.

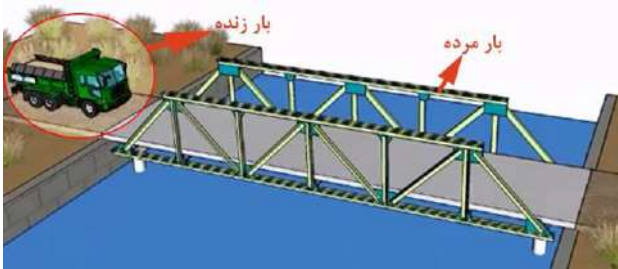


Fig. 1. Schematic view of Sardabroud Bridge

Since some coastal road bridges in Gilan, Mazandaran, and Golestan provinces with a similar structural system are still under traffic load, so the study of this type of failure, which is called progressive failure, is of considerable importance.

Progressive failure can be defined as the spread of an initial local rupture from one member to another, which ultimately leads to the failure of the entire structure or disproportionately much of it. This improper failure is due to the small initial failure caused by unforeseen events and indicates that the structural system is not able to withstand the propagation of failure due to insufficient bearing capacity.

Most truss stairs are classified as critical failure structures whose serious problem is their high vulnerability to progressive failure. Progressive failure of truss stairs can begin with rupture (tensile failure) or bending (compressive failure) of truss members. Existing standards point to three ways to reduce progressive failure. The first method is based on reducing exposure to injuries and damages. The other two methods are indirect methods and direct methods [1 and 2]. In the indirect method, failure resistance is provided by creating continuity, ductility, and increasing resistance by creating higher

indefinite degrees in the structure. In the indirect method, progressive failure resistance is provided by increasing the resistance of key structural members to specific loads or by bridging across the local failure area. The alternative load transfer method is one of the methods to investigate the progressive failure in which the critical member is removed and the structure is designed so that in case of destruction of this member, alternative routes for transfer of load from that member and bearing members around this member. Without total collapse, have additional capacity to withstand its force [1 and 2].

Liu [3] examined common European and American code design methods to prevent progressive failure due to abnormal loading. Joakim and Tavan Kim [4] investigated the progressive breakdown resistance in steel bending frames using possible alternative welding. Lou et al. [5] investigated the evaluation of frame stability index against progressive failure using push-up analysis. Weibo et al. [6] stated that the design goal in the local failure of structures that are mostly under gravity and explosive loads is focused on increasing indeterminacy and stability index to prevent local failure. In their research, they examined bridges damaged in previous earthquakes and concluded that retrofitting can increase the performance and safety of existing bridges, provided that the damage extends from the initial failure to the final sale and the effects of the structural failure mechanism. Be well considered

In this research, the performance of the Sardabroud truss bridge against impact load will be evaluated and the sensitivity of elements exposed to impact load will be studied using push-up analysis. The results show that due to the high sensitivity of the elements that are subject to impact, except for zero force elements, for other oblique and vertical elements, their damage should be properly prevented in order to prevent progressive failure. The bridge structure should be prevented.

## 2. Research method

In this paper, to determine the critical member of one of the types of truss bridges, which is called Pony Truss due to lack of bracing, the progressive failure

of Sardabroud truss bridge, which has suffered a total collapse as a result of damage to one of the vertical border elements on December 25, 2009. (Figure (2)), will be studied.

This steel bridge consists of two parallel trusses with a span of 30 meters and a height of 5 meters, the geometry, and characteristics of its sections are shown in Figures (3) and (4).



Fig. 2. the collapse of Sardabroud bridge due to heavy load collision with a key element of the structure

In this paper, to study the progressive failure of the Sardabroud Bridge, the steel truss in Abacus software is modeled in two dimensions using the Beam element.

According to the information received from the Housing and Urban Development Department of Chalous city, the total weight of the bridge is about 225 tons. Therefore, the dead load entering the middle and side nodes of the truss is about 184 and 92 kN, respectively. The live load has been applied on the bridge structure, assuming a 40-ton truck passes.

### 2.1. Validation

To evaluate the correctness of the modeling done in the software, the amount of vertical displacement of the middle node due to the 40-ton load in this node has been calculated in both numerical and analytical ways. The results extracted from the Abacus software

show that the vertical displacement of the middle node is close to 1 cm (Figure (5)).

On the other hand, using the unit load method (Equation (1)), the vertical displacement of the middle truss knot due to the presence of 40-ton load in this knot is equal to 0.78 cm.

$$1 \times \Delta = \sum \frac{nNl}{EA} \quad (1)$$

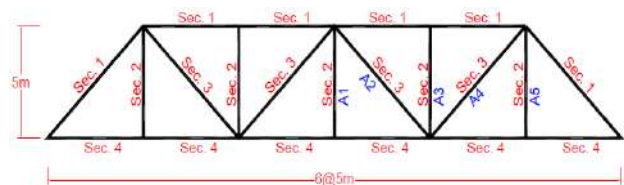


Fig. 3. Geometry of Sardabroud bridge truss

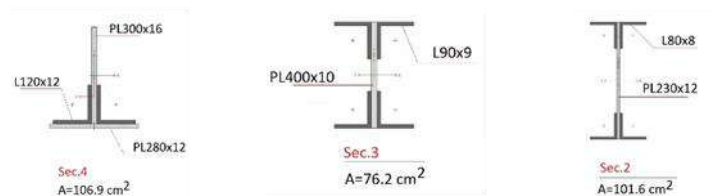


Fig. 4. Sardabroud truss bridge sections

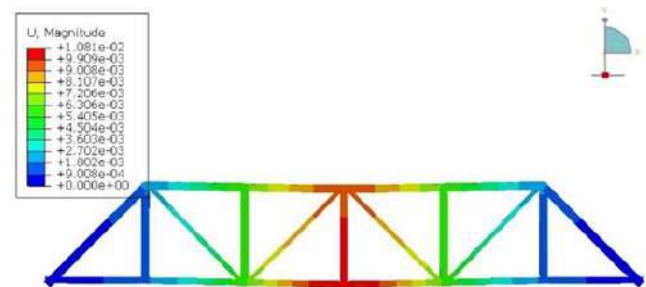


Fig. 5. Contours related to the vertical deformation of the model, during the application of a load of 40 tons to the center of the bridge.

In this regard:

- Δ Obtained deformation of the center of the bridge
- n The internal force created in each member, due to the application of a unit load of one ton applied at the center of the bridge

N internal force created in each member, due to the application of 40 ton load applied in the center of the bridge

L The length of each member

E modulus of elasticity of steel

A area of each member

As can be seen, the analytical and numerical results are about 20% different from each other, which can be considered appropriate due to the nonlinear effects in numerical modeling and the simplifying assumptions included in the analytical calculations.

## 2.2. Sensitivity analysis

Sensitivity analysis is used to determine the key element in progressive failure. This analysis is calculated based on the total capacity of the structure before and after the removal of the key element. The sensitivity index is defined using Equation (2) [7]:

$$SI = (\lambda_0 - \lambda_{\text{damage}}) / \lambda_0 \quad (2)$$

In this regard,  $\lambda_0$  is the total load capacity before removing the key element and  $\lambda_{\text{damage}}$  is the load capacity after removing the key element. The range of sensitivity index is between zero and one that the higher the sensitivity index for an element (close to one), the lower the load-bearing capacity of the structure if that member is removed; Therefore, the element with the highest sensitivity index will be the key element of the structure.

## 3. Investigation of Sardabroud bridge

### 3.1. Sensitivity of Sardabroud bridge truss elements

Due to the field visit, the load of the truck with the bridge truss is limited to vertical and oblique elements. On the other hand, according to the symmetry in the bridge structure, the sensitivity

index of the five main elements shown in Figure (3) is investigated.

To calculate the capacity of the structure, the lower end node of the removed element is gradually shifted in the vertical direction. Diagram of changes The sum of the support reaction against the vertical displacement of the end node is extracted as the capacity diagram. The maximum amount of force in the capacity diagram is considered as the load-bearing capacity of the structure; An example of a structural capacity diagram after targeting the main element A1 in Figure (3).

it has been shown; According to this figure, the capacity of the structure after the removal of A1 is equal to 1490 kN. After calculating the capacity of the structure, the sensitivity index of the main elements was calculated using Equation (2), the results of which are presented in Table (1).

As can be seen, the sensitivity index for the removal of element A3 is 0.02, which is very small; Of course, this is not far-fetched given the zero-force of this member. On the other hand, according to the sensitivity table, the adjacent elements are more than the middle elements of the bridge.

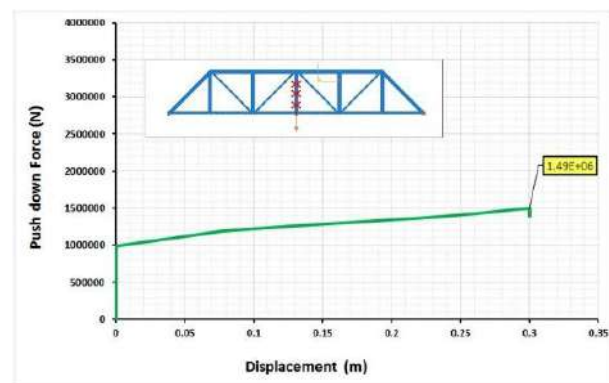


Fig. 6. Capacity diagram of Sardabroud bridge truss after removing element A1

Table 1

Sensitivity index of truss elements that are likely to be damaged when passing the truck



### 3.2. Progressive failure in Sardabroud bridge

Based on the intermediate inspection and available documents, it can be said that the heavy load of the truck hit the middle element of the truss (column A1)

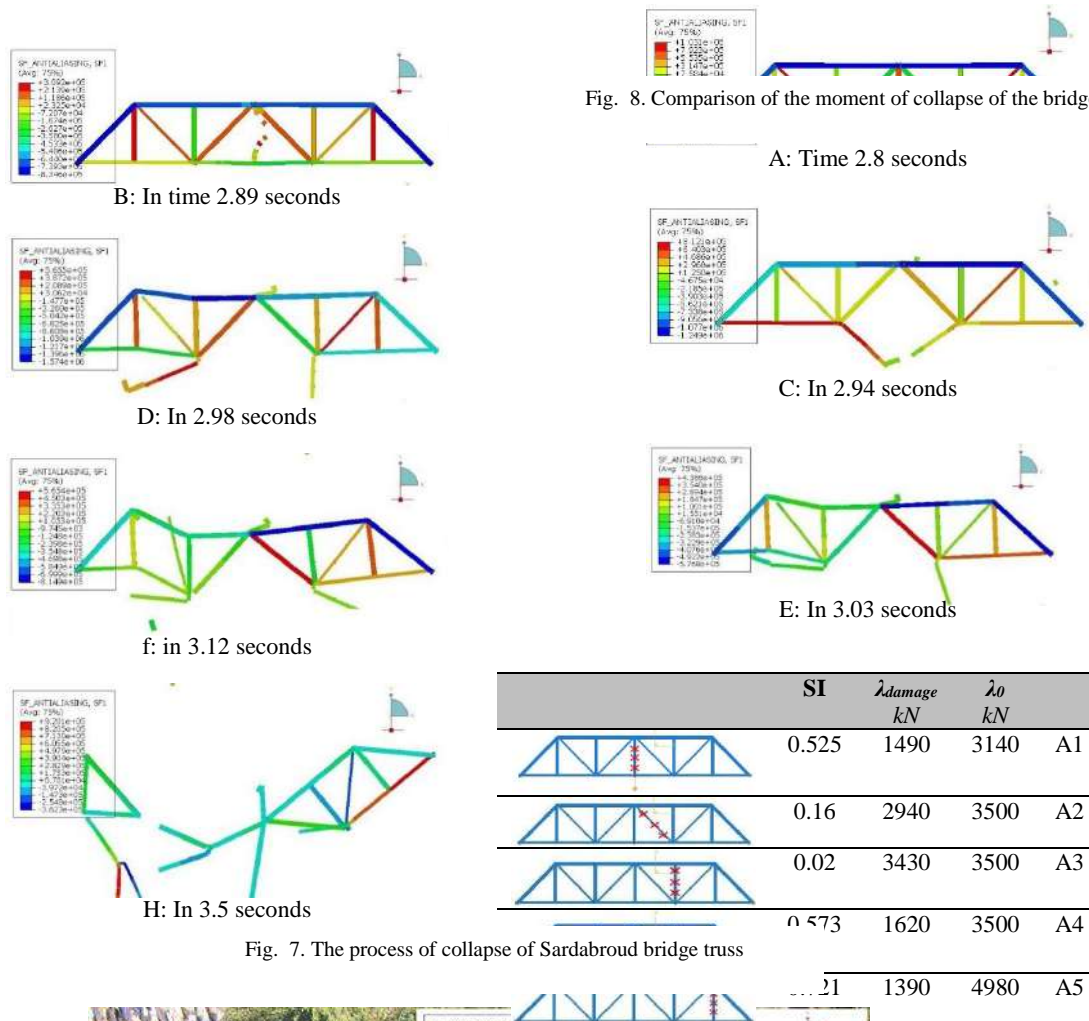
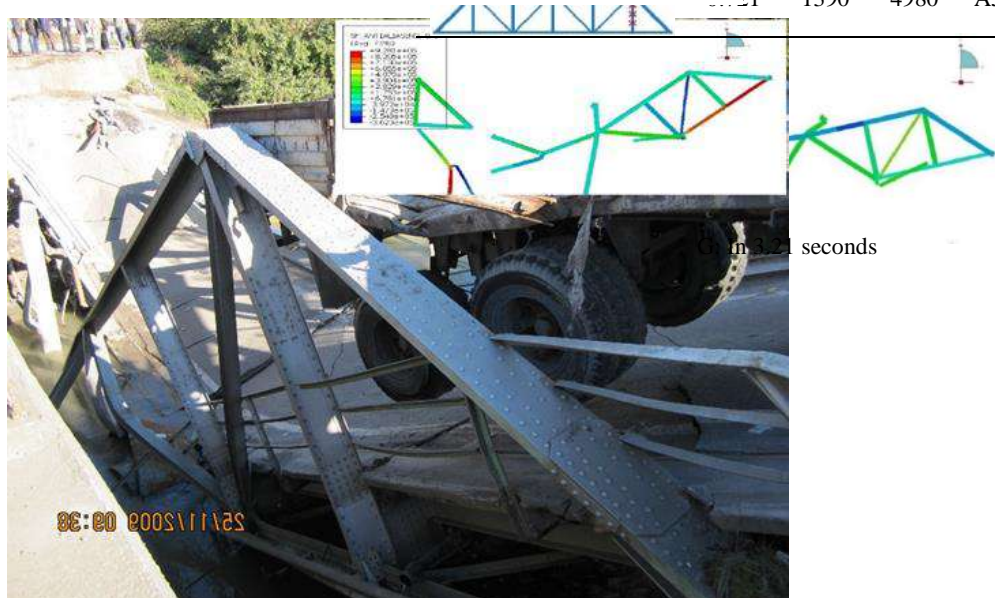


Fig. 7. The process of collapse of Sardabroud bridge truss



elements, other vertical and oblique elements can play a key role in the backward failure of the structure. Therefore, they should be prevented in appropriate ways.

## References

- [1] Saad, Ahmad, Aly Said, and Ying Tian. "Overview of progressive collapse analysis and retrofit techniques." The Proceedings of the 5th International Engineering and Construction Conference (IECC. Vol. 5. 2008. J. Newman, Electrochemical Systems, 2nd ed., Prentice-Hall, Englewood Cliffs, NJ, 1991.
- [2] Marjanishvili, Shalva, and Elizabeth Agnew. "Comparison of various procedures for progressive collapse analysis." *Journal of Performance of Constructed Facilities* 20.4 (2006): 365-374.
- [3] Lew, H. S. "Best practices guidelines for mitigation of building progressive collapse." National Institute of Standards and Technology, Gaithersburg, Maryland, USA (2003): 20899-8611.
- [4] Kim, Jinkoo, and Taewan Kim. "Assessment of progressive collapse-resisting capacity of steel moment frames." *Journal of Constructional Steel Research* 65.1 (2009): 169-179.
- Lu, Da-Gang, et al. "Robustness assessment for progressive collapse of framed structures using pushdown analysis method." *Proceeding of the 4th International Workshop on Reliable Engineering Computing*. REC. 2010.
- [6] Wibowo, Hartanto, S. Reshotkina, and D. Lau. "Modelling progressive collapse of RC bridges during earthquakes." CSCE annual general conference. 2009.
- [7] Zhang, Lei-Ming, and Xi-La Liu. "Learning from the Wenchuan earthquake: key problems in collapse analysis of structures." *Proceedings of the 14th World Conference on Earthquake Engineering*, Chinese Association of Earthquake Engineering, Beijing, China. 2008..

(Figure (2)). In the simulation process, assuming that the speed of the truck was 20 km / h (Sardabroud bridge was built on a road turn); The truck takes 5.6 seconds to cross the bridge. In other words, it is assumed that in 2.8 seconds the truck is almost in the middle of the bridge. The stress distribution corresponding to these loading conditions is shown in Figure (7-a). At this time, the impact of a heavy load on the A1 pillar causes the loss of about 50% of the capacity of the structure. As much as 0.7 seconds total breakdown will occur in the bridge truss. The process of the bridge collapse is shown in Figure.

Figure (8) compares the moment of the bridge collapse in reality with the moment of collapse simulated in Abacus software. As can be seen in both images, the five vertical and diagonal elements along with the four horizontal elements are not broken at the top and bottom edges. This shows a good fit between the simulation results and the actual process of the bridge collapse event

## 4. Result

In this paper, the collapse process of the Sardabroud truss bridge was simulated using Abacus software. The results of the software show a good agreement of the collapse simulation process with what happened. On the other hand, using sensitivity analysis, it was shown that except for zero force

## **Author Guidelines EditEdit Author Guidelines**

### **GENERAL GUIDELINES FOR AUTHORS**

Journal of civil engineering researches invites unsolicited contributions of several forms: articles, reviews and discussion articles, translations, and fora. Contributions should fall within the broad scope of the journal, as outlined in the statement of scope and focus. Contributors should present their material in a form that is accessible to a general anthropological readership. We especially invite contributions that engage with debates from previously published articles in the journal.

Submissions are double-blind peer-reviewed in accordance with our policy. Submissions will be immediately acknowledged but due to the review process, acceptance may take up to three months. Submissions should be submitted via our website submission form (see links above for registration and login). Once you login, make sure your user profile has "author" selected, then click "new submission" and follow the instructions carefully to submit your article. If problems arise, first check the FAQ and Troubleshooting guide posted below. If you are still experiencing difficulty, articles can be submitted to the editors as email attachments.

Each article should be accompanied by a title page that includes: all authors' names, institutional affiliations, address, telephone numbers and e-mail address. Papers should be no longer than 10,000 words (inclusive of abstract 100-150 words, footnotes, bibliography and notes on contributors), unless permission for a longer submission has been granted in advance by the Editors. Each article must include a 100 words "note on contributor(s)" together with full institutional address details, including email address. We request that you submit this material (title page and notes on the contributors) as "supplementary files" rather than in the article itself, which will need to be blinded for peer-review.

We are unable to pay for permissions to publish pieces whose copyright is not held by the author. Authors should secure rights before submitting translations, illustrations or long quotes. The views expressed in all articles are those of the authors and not necessarily those of the journal or its editors. After acceptance, authors and Special Issue guest editors whose institutions have an Open Access library fund must commit to apply to assist in article production costs. Proof of application will be requested. Though publication is not usually contingent on the availability of funding, the Journal is generally under no obligation to publish a work if funding which can be destined to support open access is not made available.

### **Word template and guidelines**

Our tailored Word template and guidelines will help you format and structure your article, with useful general advice and Word tips.



## **(La)TeX template and guidelines**

We welcome submissions of (La)TeX files. If you have used any .bib files when creating your article, please include these with your submission so that we can generate the reference list and citations in the journal-specific style

### **Artwork guidelines**

Illustrations, pictures and graphs, should be supplied with the highest quality and in an electronic format that helps us to publish your article in the best way possible. Please follow the guidelines below to enable us to prepare your artwork for the printed issue as well as the online version.

Format: TIFF, JPEG: Common format for pictures (containing no text or graphs).

EPS: Preferred format for graphs and line art (retains quality when enlarging/zooming in).

Placement: Figures/charts and tables created in MS Word should be included in the main text rather than at the end of the document.

Figures and other files created outside Word (i.e. Excel, PowerPoint, JPG, TIFF, EPS, and PDF) should be submitted separately. Please add a placeholder note in the running text (i.e. "[insert Figure 1.]")

Resolution: Rasterized based files (i.e. with .tiff or .jpeg extension) require a resolution of at least 300 dpi (dots per inch). Line art should be supplied with a minimum resolution of 800 dpi.

Colour: Please note that images supplied in colour will be published in colour online and black and white in print (unless otherwise arranged). Therefore, it is important that you supply images that are comprehensible in black and white as well (i.e. by using colour with a distinctive pattern or dotted lines). The captions should reflect this by not using words indicating colour.

Dimension: Check that the artworks supplied match or exceed the dimensions of the journal. Images cannot be scaled up after origination

Fonts: The lettering used in the artwork should not vary too much in size and type (usually sans serif font as a default).

### **Authors services:**

For reformatting your manuscript to fit the requirement of the Journal of Civil Engineering Researchers and/or English language editing please send an email to the following address:

researchers.services@gmail.com

Noted: There is a fixed charge for these mentioned services that is a function of the manuscript length. The amount of this charge will be notified through a reply email.

## **FAQ AND TROUBLESHOOTING FOR AUTHORS**

I cannot log in to the system. How do I acquire a new user name and password?

If you cannot remember your username, please write an email to (journals.researchers@gmail.com), who will locate your username and notify you. If you know your username, but cannot remember your password, please click the "Login" link on the left-hand menu at homepage. Below the fields for entering your username and password, you will notice a link that asks "Forgot your password?"; click that link and then enter your email address to reset your password. You will be sent an automated message with a temporary password and instructions for how to create a new password. TIP: If you do not receive the automated email in your inbox, please check your SPAM or Junk Mail folder. For any other issues, please contact our Managing Editor, Kamyar Bagherinejad (admin@journals-researchers.com).

*How do I locate the online submission form and fill it out?*

First you need to register or login (see above). Once you are logged in, make sure the "roles" section of your profile has "Author" selected. Once you assign yourself the role of "Author," save your profile and then click the "New Submission" link on your user home page.

Once you arrive at the submission form page, please read the instructions carefully filling out all necessary information. Unless specified otherwise by the editors, the journal section to be selected for your submission should be "Articles." Proceed to the remaining sections, checking all boxes of the submission preparation checklist, and checking the box in the copyright notice section (thus agreeing to journals-researchers's copyright terms). Once the first page is completed, click "Save and Continue." The next page allows you to upload your submission. Use the form to choose your file from your computer. Make sure you click "Upload." The page will refresh and you may then click "Save and Continue." You will then proceed to a page for entering the metadata for your article. Please fill out all required fields and any further information you can provide. Click "Save and Continue." The next page allows you to upload supplementary files (images, audiovisual materials, etc.). These are not required, but if you wish to provide supplementary materials, please upload them here (do not forget to click "Upload." Then click "Save and Continue." This brings you to the final page of the submission form. Please click "Finish Submission" in order to close the

submission process. You will then be notified by email that your article has been successfully submitted. TIP: If you do not receive the automated email in your inbox, please check your SPAM or Junk Mail folder. For any other issues, please contact our Managing Editor, Kamyar Bagherinejad (admin@journals-researchers.com).

*Why am I not receiving any email notifications from HAU?*

Unfortunately, some automated messages from Open Journal Systems arrive in users' Spam (or Junk Mail) folders. First, check those folders to see if the message was filtered into there. You may also change the settings of your email by editing your preferences to accept all mail from [jcer] and related journals-researchers.com email accounts.

*I am trying to upload a revised article following an initial round of peer-review, but I cannot locate where to upload the article. Where do I submit a revised article?*

Follow the login process outlined above and when you successfully login you will see on your user home page a link next to "Author" for "active" articles in our system (usually it is only one article, but if you have multiple submissions currently in our system, the number could be higher. Click the "Active" link and you will be led to a page that lists your authored articles currently in our system. Click the link under the column labeled "Status" and this will take you to a page showing the current review status of your article. At the very bottom of the screen, you will see an upload form under the heading "Editor decision." Here you may upload your revised article. An automated email will be sent to the editors and you may also notify them directly via email. You may then logout.

I successfully submitted an article; how long will it take for the editors to respond to me with a decision.

For all articles that are recommended for peer-review, the editors of JCER strive to notify authors of a decision within 4-6 weeks. You may contact JCER's Managing Editor, Kamyar Bagherinejad (admin@journals-researchers.com). if you have any questions relating to the review process and its duration.

For all other inquiries, please contact: Kamyar Bagherinejad (Managing Editor)

## Privacy Statement

The names and email addresses entered in this journal site will be used exclusively for the stated purposes of this journal and will not be made available for any other purpose or to any other party.

## Articles

Section default policy

Make a new submission to the Articles section.

## Copyright Notice EditEdit Copyright Notice

Journal of Civil Engineering Researchers follows the regulations of the International Committee on Publication Ethics (COPE) and the ethical principles of publishing articles in this journal are set based on the rules of this committee, and in case of problems, it will be treated according to these rules.

This work is licensed under a Creative Commons Attribution 4.0 International License (CC BY 4.0).

In short, copyright for articles published in this journal is retained by the authors, with first publication rights granted to the journal. By virtue of their appearance in this open access journal, articles are free to use, with proper attribution and link to the licensing, in educational, commercial, and non-commercial settings

## Privacy Statement EditEdit Privacy Statement

The names and email addresses entered in this journal site will be used exclusively for the stated purposes of this journal and will not be made available for any other purpose or to any other party.

# Scholars Pavilion



**Scholars Pavilion** or **Scholars Chartagi** is a monument donated by the Islamic Republic of Iran to the United Nations Office at Vienna. The monument architecture is claimed by the Islamic Republic News Agency of Iran to be a combination of Islamic and Achaemenid architecture, although the latter clearly predominates in the decorative features, with Persian columns and other features from Persepolis and other remains from the Achaemenid dynasty. The Chahartaq pavilion form runs through the architecture of Persia from pre-Islamic times to the present.

Statues of four famous Persian medieval scholars, Omar Khayyam, Al-Biruni, Muhammad ibn Zakariya al-Razi and Ibn-Sina are inside the pavilion. This monument donated in June 2009 in occasion of Iran's peaceful developments in science.



**J-Researchers**